

### Key Points:

- A high-resolution wave-current coupled 3D model was applied to investigate monthly and episodic lake dynamics of summer circulation
- Wind and density-driven currents dominate circulation while rivers, straits, waves, model grids, and topography modify it to some extent
- Simulated anticyclonic gyres in the southern basin are dominated by winds and baroclinic dynamics and influenced by lake bathymetry

### Correspondence to:

M. Xia,  
mxia@umes.edu

### Citation:

Mao, M., & Xia, M. (2020). Monthly and Episodic Dynamics of Summer Circulation in Lake Michigan. *Journal of Geophysical Research: Oceans*, 124, e2019JC015932. <https://doi.org/10.1029/2019JC015932>

Received 3 DEC 2019

Accepted 10 MAY 2020

Accepted article online 16 MAY 2020

## Monthly and Episodic Dynamics of Summer Circulation in Lake Michigan

Miaohua Mao<sup>1</sup>  and Meng Xia<sup>2</sup> 

<sup>1</sup>CAS Key Laboratory of Coastal Environmental Processes and Ecological Remediation, Yantai Institute of Coastal Zone Research, Chinese Academy of Sciences, Yantai, Shandong, P.R. China, <sup>2</sup>Department of Natural Sciences, University of Maryland Eastern Shore, Princess Anne, MD, USA

**Abstract** A comprehensive understanding of lake circulation is fundamental to inform better management of ecological issues and fishery resources in the Great Lakes. In this study, a high-resolution, wave-current coupled, three-dimensional modeling system was applied to investigate the monthly and episodic dynamics of summer circulation in Lake Michigan. Model sensitivities to three wind sources and two grid resolutions against observed current velocities, water temperatures, and significant wave heights in the summer of 2014 were examined. Model performance was validated with additional satellite imagery and current measurements in the summer of 2015. Results indicated that the high-resolution model driven by the observation-based winds reproduced lake dynamics most reasonably. In July 2014, a pair of monthly averaged anticyclonic (i.e., clockwise) gyres in the surface layer were simulated in southern Lake Michigan. Analysis indicates that they originate from the wind-driven, upwelling-favorable, jet-like Ekman currents along the west shore, which are connected by the density-driven basin-scale circulation. Although river inputs, strait exchanges, waves, grid resolutions, and bathymetric variations influence the monthly surface circulation, their effects are less important than the wind and density-driven currents. Additional simulations support the predominant impacts of wind and density-driven currents on lake surface circulation during a strong wind event. Further investigations suggest that lake circulation varies from surface to bottom layers, and this knowledge is significant to the related ecological issues and fishery resources management. The numerical model configured to Lake Michigan is beneficial to understanding dynamics in the Great Lakes system and other large water bodies.

**Plain Language Summary** Water movements in freshwater and estuarine environments are particularly relevant to fisheries recruitment, as reproductive success of fish and invertebrate populations is usually determined by physical factors influencing their sensitive early life stages. Predicting the complex water currents in a precise way is thus of great importance to the scientific and fishery communities. In this paper, we used a collection of observed data including the measured wind speed, water velocity, water temperature, and wave height to help adjust the parameters in the computer program and improve the model's ability of predicting the 2014 summer circulation in Lake Michigan. Based on the established modeling system, it is indicated that both monthly and episodic lake currents are mostly influenced by winds and heat flux. After doing further “what-if” simulations in the computer programs, we find that adjacent rivers and lakes, nearshore wave activities, and lake bathymetry can also affect lake surface circulation to some extent. At a monthly timescale, the computer program simulated a pair of circular movements in a clockwise direction over the southern lake, which are attributed to the combined actions of wind-induced coastal jets and basin-scale circulation driven by the spatially non-uniform lake temperatures. Simulated maps of water movements in the summer can potentially help lake and coastal communities expect the hot spot of fish larvae, track, and trace their passive movements driven by lake currents.

### 1. Introduction

Given that wind is one of the most important forces in generating lake currents, effects of wind stress on various types of gyre circulation (e.g., single or double cyclonic/anticyclonic) have been addressed by international lake research communities for both small and large lakes worldwide. The circulation patterns in Lake Tahoe (USA) and Lake Belau (Northern Germany) are all consistent with their wind stress curls, for example, anticyclonic and cyclonic, respectively (Podsetchine & Schernewski, 1999; Strub & Powell, 1986). Additionally, Schoen et al. (2014) demonstrated that winds play an important role in the switches of gyre rotation, which are directly related to the wind direction over the shallow St. Lucia

(South Africa). Troitskaya et al. (2015) suggested that the wind magnitude is substantial to the intensification and stabilization of the cyclonic summer currents in the large Lake Baikal (East Siberia). Wu et al. (2018) further indicated that under different wind conditions (e.g., strong vs. low or medium), the structure of lake circulation varied significantly (e.g., uniform currents through the water column vs. wind-driven surface currents compensated by bottom reversal ones).

Due to similarities of lake dynamics, the importance of winds to lake currents has been widely confirmed in the Great Lakes system (Bai et al., 2013; Beletsky et al., 1999). Since the pioneering work of Rao and Murty (1970) on the wind-driven circulation in Lake Ontario, dynamics of the Great Lakes have been investigated using numerical models and chronically under-observed measurements (Beletsky & Schwab, 2008; Niu & Xia, 2017; Schwab & Beletsky, 2003). By analyzing velocity data collected from the acoustic Doppler current profiler (ADCP) and vector-averaging current meters, Beletsky et al. (1999) summarized that the basin-scale gyre circulation is primarily driven by winds in winter, while it is highly associated with thermal structures in summer for large lakes in the Great Lakes system. Based on the simulated summer circulation of Lake Michigan, Beletsky and Schwab (2001) illuminated that the current intensity and its cyclonic (i.e., anticlockwise) vorticity are directly associated with the wind stress strength and temperature gradients. Schwab and Beletsky (2003) further quantified the contribution of individual forcing to the vorticity tendency and concluded that the cyclonic wind stress curl,  $\frac{\partial \tau_y}{\partial x} - \frac{\partial \tau_x}{\partial y}$ , where  $(\tau_x, \tau_y)$  is the wind stress in the  $(x, y)$  plane, and baroclinicity (i.e., lake temperature gradients driven by air-sea heat flux) control the gyre circulation in winter and summer, respectively.

Considering the dominant roles of wind and density-driven flows in the Great Lakes and complexity of coastal geometry and circulation, subsequent studies (Beletsky et al., 2013; Mao & Xia, 2017; Niu et al., 2015) indicated that various selections of wind sources and grid resolutions likely affect the accuracy of hydrodynamic simulations. By replacing the observation-based wind field interpolated from limited buoys with the atmospherically modeled products, Beletsky et al. (2003) modeled the coastal current more accurately under stormy conditions. In addition, model performance in the coastal upwelling simulation was improved by refining the grid size from 5 to 2 km, allowing for the simulation of an anticyclonic (i.e., clockwise) gyre in southern Lake Michigan (Beletsky et al., 2006). With a high grid resolution (2–4 km) applied near the Keweenaw coast of Lake Superior, Chen et al. (2001) stated that the anticyclonic gyre was related to the baroclinic instability of the adjacent coastal jet. Although Chen et al. (2001) revealed the complex mechanism of the anticyclonic gyre during the summer months, it was conducted under an idealized wind condition. Given that the forcing mechanism of the anticyclonic gyre under realistic wind conditions remains only partially understood, it is worthwhile to further explore how wind and density-driven currents influence the gyre's intensity, size, and shape.

Although the general gyre circulation in the Great Lakes had previously been well studied using numerical models (Allender, 1977; Beletsky et al., 1999), little attention was paid to the wave effects, which were substantial to coastal circulation (Bolaños et al., 2014). Given the similarity of coastal dynamics, the wave-induced circulation in the nearshore of the Great Lakes is likely significant and requires further investigations (Rao & Schwab, 2007). Previous studies using the wave-current coupled model provided encouraging results, but it was either applied to shallow bays (Mao & Xia, 2018; Olabarrieta et al., 2011) or during episodic events (Mao & Xia, 2017). Circulation dynamics have seldom been evaluated on a regional-scale  $O(100 \text{ km})$  domain or at a longer timescale. A few studies indicated that wave effects on circulation are substantial, both at episodic and seasonal timescales in the shallow Lake Erie (Niu & Xia, 2017). Considering distinctive geographical features and unique mean circulation patterns in each of the Great Lakes (Beletsky et al., 1999), it is worthwhile to extend understanding of the lake-wide circulation (e.g., dynamics of gyre circulation and wave effects on nearshore currents) at various timescales in the relatively large and deep lake (e.g., Lake Michigan).

In this study, a high-resolution, three-dimensional, unstructured grid, finite-volume community ocean model (FVCOM) (Chen et al., 2013), which had been widely used in the Great Lakes (Anderson & Schwab, 2017; Niu et al., 2018; Xue et al., 2017), was applied to Lake Michigan. To include wave effects on lake circulation, this hydrodynamic model was offline coupled with the wave model simulating waves nearshore (SWAN) (Zijlema, 2010). Remaining sections of this manuscript are organized as follows.

Section 2 introduces the methodology, which includes the model description, data sources and model inputs, experimental design, and skill metrics. Section 3 examines the model sensitivity to three wind sources and two grid resolutions, followed by the model validation and the discussion of the monthly lake circulation and the forcing mechanism of gyre circulation in summer. The major conclusions are summarized in section 4.

## 2. Methodology

### Model Domain and Grid

Lake Michigan (Figure 1a) is the third largest lake in the Great Lakes system by surface area (58,000 km<sup>2</sup>). Its narrow and elongated body extends for a length of 494 km (latitude 41.6–46.1°N) and a width of 190 km (longitude 88.1–84.4°W), with mean and maximum water depths of 85 and 281 m, respectively. This semi-enclosed water body communicates with Lake Huron via Straits of Mackinac in its northeastern corner. In addition to applying the realistic meteorological forcing, the bi-lake exchanges were specified by using the hourly water surface elevation as open boundary conditions. It was retrieved from the National Oceanic and Atmospheric Administration (NOAA) and National Ocean Service (NOS) at Mackinaw City, Michigan. Although a bi-lake model would be the best one to resolve strait exchanges, the single-lake model was adopted since it is sufficient to capture the exchanging flows with proper open boundary conditions (Mao & Xia, 2017) and saves the computational time, particularly for the wave-current coupled model. Recent studies by Rowe et al. (2015, 2017) supported that the one-lake model is capable of achieving satisfactory results for the summer circulation of Lake Michigan. The lake's major body includes Chippewa Basin, South Fox Island, Mid-Lake Plateau, and South Chippewa Basin. Green Bay is located on the left flank of Chippewa Basin.

To accurately resolve the multiscale bathymetry and dynamics with an expedient computational effort, hydrodynamic simulations from the high and medium-resolution (HR and MR; 38,324 and 9,581 elements, and 20,108 and 5,256 nodes) models (Figures 1b and 1c) were compared against observations. The grid size of the HR model is 3.8 km in the mid-lake area, which is refined to 210 m near the coast and islands. Overall, size of the MR grid is twice that of the HR model over the entire domain. Considering the numerical stability, the finest resolutions were applied around the South Fox Island to follow the highly complex island lines. Given that the baroclinic Rossby radius (Beletsky et al., 1997, 2006) within the 8–10 km coastal boundary layer (Murthy & Dunbar, 1981) is less than 5 km, the HR and MR grids along the west shore, where the monthly averaged jet-like currents develop (section 3.3.1), are set at 1.1–1.5 and 2.2–2.8 km, respectively. Computational speeds of the MR model in simulating wave and circulation are 1.25 and 0.94 simulated days/computing hour, which decrease to 1/5 and 1/3, respectively (i.e., computational hours increase to five and three times for the same simulation period), by using the HR one. The number of processors used in the parallel execution are 16 in the Stampede high-performance computing machines and 72 in the Cheyenne system. The Lake Michigan hydrodynamic model selected 20 uniform sigma layers in the terrain-following vertical coordinate (e.g., the vertical resolution is  $\frac{1}{20}$  of the local water depth, which is less than 14 m at the deepest location of the lake) based on the model sensitivity experiments described in section 3.1.

### 2.2. Wave-Current Coupled Model

The unstructured grid model simulating waves nearshore (SWAN), in which the spatial distribution of the grid structure is the same as that in the hydrodynamic model, has been successfully configured to Lake Michigan by Mao et al. (2016). The wave action spectral energy conservation in the SWAN model considers the local and spatial variations, depth and current-induced refraction and frequency shift, wind input, non-linear wave-wave interactions, whitecapping, bottom friction, and depth-induced breaking. The model is discretized with a first order, backward-space, backward-time scheme. The hybrid central scheme is used in the wave spectral space. Wave directions in this finite-difference-based model are applied with a full sector (i.e., 0–360°), which are resolved evenly into 36 bins. Wave frequencies are discretized over 32 bins with an increasing logarithmic scale, which range from 0.0512 to 1 Hz. Formulations of the wind input function and whitecapping dissipation derive from Janssen (1991) and readjusted Rogers et al. (2003), respectively. The depth-induced wave-breaking term adopts the bore-based model of Thornton and Guza (1983). Detailed physics settings of the Lake Michigan wave model are referred to in Mao et al. (2016).



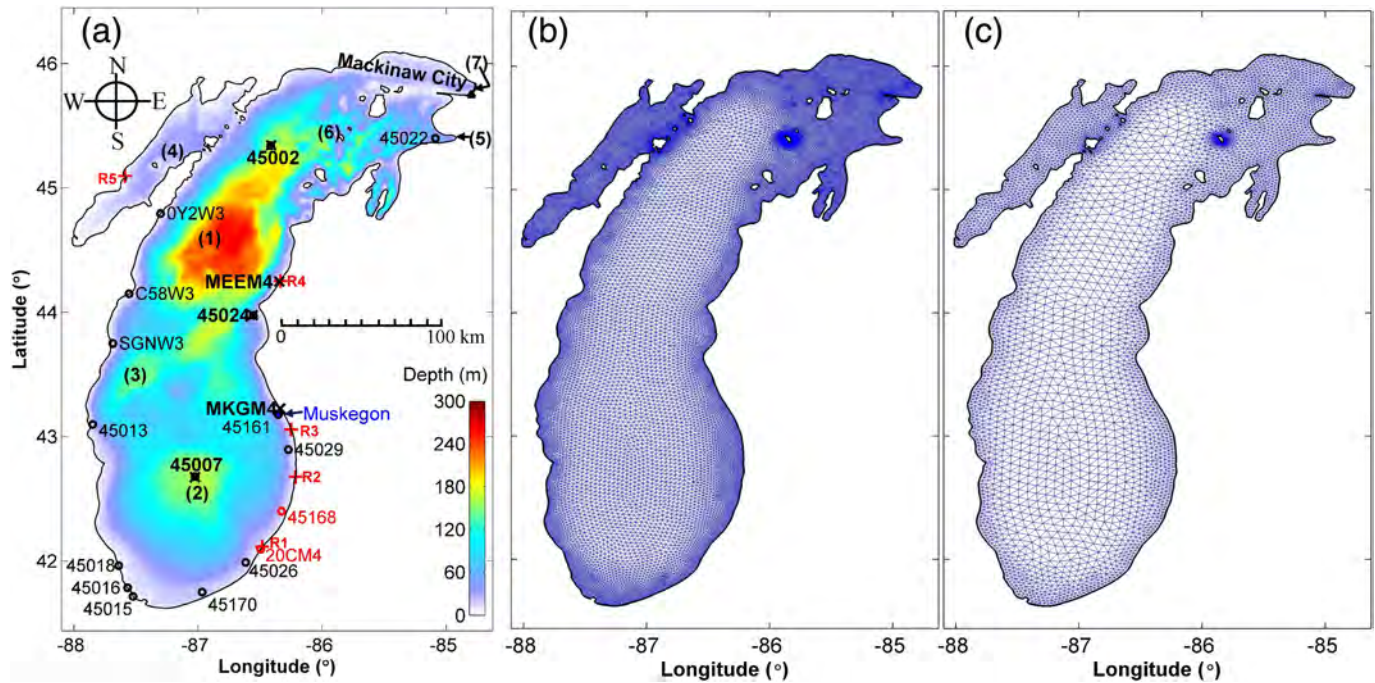


**Figure 1.** (a) Bathymetry, locations of observations, critical geographic names, and river and strait boundary locations in Lake Michigan; (b) high and (c) medium-resolution grids. In panel (a), black crosses and open circles represent wind data and surface temperature stations from the NDBC. The open boundary layer along the Straits of Mackinac is indicated with the solid black line in the northeastern corner of the lake, and the nearby triangle is the location of the NOS gauge. Red plus signs and the blue dot denote river flows collected from the USGS and ADCP-measured currents at Muskegon, MI. Buoy stations for wave data are the same as those for surface temperatures, except for that 45013 and SGNW3 are replaced by 45168 and 20CM4 (red open circles). Geographic names include (1) Chippewa Basin, (2) South Chippewa Basin, (3) Mid-Lake Plateau, (4) Green Bay, (5) Little Traverse Bay, (6) South Fox Island, and (7) Straits of Mackinac. River inputs include R1 (St. Joseph River), R2 (Kalamazoo River), R3 (Grand River), R4 (Manistee River), and R5 (Menominee River).

The hydrodynamic model configured to Lake Michigan (Mao & Xia, 2017) is the free surface, three-dimensional (3D), primitive equation based, unstructured grid, finite-volume community ocean model (FVCOM). To resolve the complex bathymetry and multiscale dynamics, unstructured grids in the horizontal space and terrain-following sigma layers in the vertical coordinate are employed. FVCOM is integrated using a mode-split solver, in which the external and internal calculations are advanced at 4- and 16-s time steps. The vertical and horizontal mixing processes are handled by the modified MY-2.5 turbulence closure model (Galperin et al., 1988) and eddy parameterization scheme (Smagorinsky, 1963). Hydrostatic and Boussinesq assumptions are adopted so that density variations are neglected, except for the term multiplied by gravity in the buoyancy force. The horizontal diffusion and bottom roughness are set at a multiplier of 0.1 and a constant length of 0.1 cm. The air-sea transfers of heat and momentum fluxes are achieved via the lake's surface boundary layer. The net heat flux ( $H_{FLX}$ ) is calculated by using atmospheric variables including wind speed, air temperature ( $T_a$ ), lake surface temperature, relative humidity, downward shortwave ( $SW_{down}$ ), downward longwave ( $LW_{down}$ ), and upward longwave radiation fluxes ( $LW_{up}$ ). The  $H_{FLX}$  budget model is calculated as:

$$H_{FLX} = SW_{down} + LW_{down} + LW_{up} + H_{sensible} + H_{latent} \quad (1)$$

The  $SW_{down}$  and  $LW_{down}$  data were collected from the Global Environmental Multiscale Model (Côté et al., 1998), which were interpolated to computational cells for calculation. The  $\sigma$  used in the upward longwave radiation stress expression  $LW_{up} = -\sigma T_a^4$  represents the Stefan-Boltzmann constant ( $5.67 \times 10^{-8} \text{ W m}^{-2} \text{ K}^{-4}$ ). The sensible ( $H_{sensible}$ ) and latent ( $H_{latent}$ ) heat transfers were collected on the basis of the bulk aerodynamic formulation COARE 2.6 developed by Fairall et al. (1996).

The one-way, wave-current offline coupling procedure is described as follows. Driven by surface winds, SWAN produces wave parameters including the significant wave height, peak wave period, mean wave direction, mean wavelength, and bottom wave orbital velocity and period, which are further passed to FVCOM for the computation of the wave-induced circulation (Qi et al., 2009). The computational time

step of the wave model is set to 5 min, and the coupling processes are taken hourly. The wave and hydrodynamic models in the system use identical horizontal grids so that interpolating errors due to the inconsistency of grids are avoided. Wave effects on circulation include the Stokes drift  $\vec{u}_{st}$  (Phillips, 1977), wave-induced radiation stress (Mellor, 2015) and roller (Svendsen et al., 2002), wave-altered sea surface roughness (Donelan et al., 1993), and bottom stress (Madsen, 1994). Stokes drift and Stokes-Coriolis force  $\vec{u}_{st}$  are included in the continuity and momentum balance by switching on the option of wave-current interaction in the standard FVCOM. The Coriolis frequency  $f$  is equal to twice the Earth rotation rate  $\Omega$  ( $7.2921 \times 10^{-5}$  rad/s) multiplied by the latitude  $\varphi$  ( $f = 2\Omega \sin \varphi$ ).

In a generalized terrain-following coordinate system, the governing equation of momentum, continuity, temperature, salinity, and density with the inclusion of wave-induced effects are given as follows:

$$\frac{\partial u D}{\partial t} + \frac{\partial u^2 D}{\partial x} + \frac{\partial uv D}{\partial y} + \frac{\partial u \omega}{\partial \hat{\sigma}} - f v D = -D \frac{\partial}{\partial x} (g \eta + p_{atm}) - D \int_{\hat{\sigma}}^0 \left( D \frac{\partial \rho}{\partial x} - \hat{\sigma} \frac{\partial D \partial \rho}{\partial x \partial \hat{\sigma}} \right) d\hat{\sigma} - \left( \frac{\partial D S_{xx}}{\partial x} + \frac{\partial D S_{xy}}{\partial y} \right) + \hat{\sigma} \left( \frac{\partial D \partial S_{xx}}{\partial x \partial \hat{\sigma}} + \frac{\partial D \partial S_{xy}}{\partial y \partial \hat{\sigma}} \right) + \frac{\partial \tau_x}{\partial \hat{\sigma}} \quad (2)$$

$$\frac{\partial v D}{\partial t} + \frac{\partial uv D}{\partial x} + \frac{\partial v^2 D}{\partial y} + \frac{\partial v \omega}{\partial \hat{\sigma}} + f u D = -D \frac{\partial}{\partial y} (g \eta + p_{atm}) - D \int_{\hat{\sigma}}^0 \left( D \frac{\partial \rho}{\partial y} - \hat{\sigma} \frac{\partial D \partial \rho}{\partial y \partial \hat{\sigma}} \right) d\hat{\sigma} - \left( \frac{\partial D S_{xy}}{\partial x} + \frac{\partial D S_{yy}}{\partial y} \right) + \hat{\sigma} \left( \frac{\partial D \partial S_{xy}}{\partial x \partial \hat{\sigma}} + \frac{\partial D \partial S_{yy}}{\partial y \partial \hat{\sigma}} \right) + \frac{\partial \tau_y}{\partial \hat{\sigma}} \quad (3)$$

$$\frac{\partial D u}{\partial x} + \frac{\partial D v}{\partial y} + \frac{\partial \omega}{\partial \hat{\sigma}} + \frac{\partial \eta}{\partial t} = 0, \quad (4)$$

$$\frac{\partial \theta D}{\partial t} + \frac{\partial \theta u D}{\partial x} + \frac{\partial \theta v D}{\partial y} + \frac{\partial \theta \omega}{\partial \hat{\sigma}} = \frac{1}{D} \frac{\partial}{\partial \hat{\sigma}} \left( K_h \frac{\partial \theta}{\partial \hat{\sigma}} \right) + D \hat{H} + D F_{\theta} \quad (5)$$

$$\frac{\partial s D}{\partial t} + \frac{\partial s u D}{\partial x} + \frac{\partial s v D}{\partial y} + \frac{\partial s \omega}{\partial \hat{\sigma}} = \frac{1}{D} \frac{\partial}{\partial \hat{\sigma}} \left( K_h \frac{\partial s}{\partial \hat{\sigma}} \right) + D F_s \quad (6)$$

$$\rho = \rho(\theta, s), \quad (7)$$

where  $(x, y)$  and  $\hat{\sigma}$  are the horizontal and vertical axes of the generalized terrain-following coordinate;  $t$  is the time;  $(u, v)$  and  $\omega$  are the current velocities in the  $(x, y)$  and  $\hat{\sigma}$  planes, where  $(u, v)$  are the summations of Stokes drifts ( $u^{st}, v^{st}$ ) and Eulerian velocities ( $u^E, v^E$ );  $(\tau_x, \tau_y)$  are the stresses in the  $(x, y)$  plane;  $g$  is the gravity constant of  $9.8 \text{ m/s}^2$ ; the total water depth  $D = h + \eta$  includes the mean water depth  $h$  and sea surface elevation  $\eta$ ;  $\theta$ ,  $s$ , and  $\rho$  are the potential temperature, salinity, and density, respectively;  $p_{atm}$  is the air pressure;  $\hat{H}$  is the solar irradiance;  $K_h$  is the thermal vertical eddy diffusion coefficient;  $F_{\theta}$  and  $F_s$  represent the thermal and salt diffusion terms, respectively.

$(S_{xx}, S_{yy}, S_{xy})$  are the latest 3D radiation stress (Mellor, 2015) and roller (Svendsen et al., 2002) terms implemented to the coupled system, which corrected previous errors in treating the wave pressure properly (Mellor, 2003) and replaced the surface-intensified delta function (Mellor, 2008) in the previous FVCOM versions. The mathematical expressions are written as follows:

$$\begin{cases} S_{xx} = kE \left( \frac{k_x k_x}{k^2} F_{CC} F_{CS} - F_{SS} F_{SC} \right) + \frac{E}{2D} \Im(\zeta) + \frac{k_x k_x}{k} \frac{C^2}{L} A_R R_z \\ S_{yy} = kE \left( \frac{k_y k_y}{k^2} F_{CC} F_{CS} - F_{SS} F_{SC} \right) + \frac{E}{2D} \Im(\zeta) + \frac{k_y k_y}{k} \frac{C^2}{L} A_R R_z \\ S_{xy} = \frac{k_x k_y}{k^2} F_{CC} F_{CS} + \frac{k_x k_y}{k} \frac{C^2}{L} A_R R_z. \end{cases} \quad (8a)$$

$$\Im(\zeta) = \frac{\partial}{\partial \zeta} (2F_{CC} F_{SS} - F_{SS}^2) \quad (8b)$$

$$\begin{cases} F_{SS} = \frac{\sinh kD(1 + \zeta)}{\sinh kD} \\ F_{SC} = \frac{\sinh kD(1 + \zeta)}{\cosh kD} \\ F_{CS} = \frac{\cosh kD(1 + \zeta)}{\sinh kD} \\ F_{CC} = \frac{\cosh kD(1 + \zeta)}{\cosh kD}. \end{cases} \quad (8c)$$

$E$  and  $k$  are the wave energy and wave number;  $(k_x, k_y)$  are components of the wave number in  $(x, y)$  space; the sigma value  $\zeta = \frac{z - \hat{\eta}}{D}$  varies from  $-1$  to  $0$  with a corresponding vertical location  $z$  from bottom  $-h$  to the phase-averaged water surface  $\hat{\eta}$ , and the vertical integration of  $\Im(\zeta)$  through the water column is  $\int_{-1}^0 \Im d\zeta = 1$ . The wave-induced roller decays exponentially from surface to bottom according to the vertical distribution function  $R_z$  (Svendsen et al., 2002).

When switching on the option of wave-current interaction in the standard FVCOM, combined wave-averaged bottom stress  $\tau_{cw}$  in the current direction parameterized by Soulsby (1997) was calculated:

$$\tau_{cw} = \tau_c \left[ 1 + 1.2 \left( \frac{\tau_w}{\tau_c + \tau_w} \right)^{3.2} \right] \quad (9a)$$

where the bottom frictional stresses  $(\tau_{bx}, \tau_{by})$  due to current  $(\tau_{cx}, \tau_{cy})$  and wave  $(\tau_{wx}, \tau_{wy})$  are calculated based on the wave-current boundary model (Madsen, 1994):

$$(\tau_{bx}, \tau_{by}) = \tau_{cw}(u_c, v_c) / \sqrt{u_c^2 + v_c^2} \quad (9b)$$

$$(\tau_{cx}, \tau_{cy}) = \rho C_d(u_c, v_c) \sqrt{u_c^2 + v_c^2} \quad (9c)$$

$$(\tau_{wx}, \tau_{wy}) = 0.5 f_w(u_w, v_w) \sqrt{u_w^2 + v_w^2} \quad (9d)$$

Herein,  $(u_c, v_c)$  and  $(u_w, v_w)$  are the current velocity and wave orbital velocity near the bottom in  $(x, y)$ , respectively.  $C_d$  is the bottom drag coefficient, and  $f_w$  is the wave friction factor dependent upon the relative roughness.

Surface wind stresses  $(\tau_{sx}, \tau_{sy})$  are directly proportional to wind drag coefficient  $C_D$  by  $(\tau_{sx}, \tau_{sy}) = \rho_{air} C_D (u_{10}^2, v_{10}^2)$ , where  $\rho_{air}$  is the air density at  $1.293 \text{ kg/m}^3$  and  $(u_{10}, v_{10})$  are the  $(x, y)$  components of wind speed at 10-m height  $U_{10}$ . In the standard FVCOM,  $C_D$  is a piecewise function of  $U_{10}$  (Large & Pond, 1981):

$$C_D = \begin{cases} 1.2 \times 10^{-3} & U_{10} < 11 \text{ m/s} \\ (0.49 + 0.065 \times U_{10}) \times 10^{-3} & 11 \text{ m/s} \leq U_{10} \leq 25 \text{ m/s} \\ 2.115 \times 10^{-3} & U_{10} > 25 \text{ m/s} \end{cases} \quad (10a)$$

In the modified wave-current coupled model,  $C_D$  is associated with sea surface roughness  $z_{0s}$  (Donelan et al., 1993) and expressed as:

$$C_D = \left[ \frac{\kappa}{\ln(10/z_{0s})} \right]^2 \quad (10b)$$

$$z_{0s} = \begin{cases} 3.7 \times 10^{-5} \cdot \frac{U_{10}^2}{g} \left( \frac{U_{10}}{C_p} \right)^{0.9} & \frac{U_{10}}{C_p} < 10 \\ 3.7 \times 10^{-5} \cdot \frac{U_{10}^2}{g} 10^{0.9} & \frac{U_{10}}{C_p} \geq 10. \end{cases} \quad (10c)$$

$z_{0s}$  is related to the inversed wave age  $\frac{U_{10}}{C_p}$  with an upper boundary value of 0.002 (Ardhuin et al., 2008).  $C_p$  is the wave phase speed, and  $\kappa$  is the von Kármán constant of 0.41.

### 2.3. Data Sources and Model Inputs

Model bathymetry was retrieved from the NOAA's National Geophysical Data Center (NGDC) six arc-sec data. Three wind field sources used for comparisons include the Great Lakes Environmental Research Laboratory's observation-based hourly data processed using the Natural Neighboring Method (NNM) (Lang & Leshkevich, 2014; Schwab & Morton, 1984), Canadian Meteorological Centre's three-hourly, 10-km product from the Global Environmental Multiscale (GEM) model (Côté et al., 1998), and the hourly reanalyzed dataset gridded at  $0.2^\circ$  from the Climate Forecast System Version 2 (CFSv2) (Saha et al., 2014). Air temperature and pressure, relative humidity, and downward shortwave and longwave radiation fluxes were from the GEM. Hourly water surface elevation at Mackinaw City, Michigan, and daily river discharges were collected from the NOS and United States Geological Survey (USGS), respectively. Five major river

flows (i.e., Grand, St. Joseph, Menominee, Kalamazoo, and Manistee Rivers) in the summer of 2014 account for 27%, 19%, 19%, 12%, and 12% of the discharge included in the model (e.g., 404 m<sup>3</sup>/s). The hourly wind data at the coastal stations MKGM4, 45,024, and MEEM4 and mid-lake buoys 45,002 and 45,007 are managed by the NOAA's National Data Buoy Center (NDBC).

Surface temperature and wave data used for the model sensitivity experiments are available from 15 NDBC buoys. Records of the ADCP surface current data at 30-min time intervals from station Muskegon, Michigan, are primarily maintained by Mr. Steven Ruberg of the Great Lake Environmental Research Laboratory's (GLERL) Realtime Coastal Observation Network (ReCON). Detailed information of observations available in 2014 is provided in Figure 1a and Table 1. Additional data for model validation in the summer (i.e., July–September) of 2015 includes the monthly averaged lake surface temperatures derived from the National Aeronautics and Space Administration's (NASA) Aqua Moderate-Resolution Imaging Spectroradiometer (MODIS) satellite imagery gridded at 0.042° (e.g., 4.6 and 3.3 km along the lake's longitudinal and latitudinal axes, respectively). The ADCP-recorded vertical profile of horizontal currents at 30-min time intervals is available near the mid-west shore at station NDBC 45013, which is owned and maintained by University of Wisconsin-Milwaukee Buoy. The local water depth of this station is 20 m, and the profile of current velocity data are available at a 2-m spatial interval from surface to bottom, with the top layer being located at 1 m below the water surface.

#### 2.4. Design of Numerical Experiments

Hydrodynamic sensitivities to three wind sources and two grid resolutions were examined in the summer of 2014 by comparing the simulated surface current and temperature with the ADCP measurement and NDBC buoys. The baseline FVCOM (case A3) was driven by the spatially varying NNM winds with the inclusion of river inputs, strait exchanges, and waves. Simulations with either the alternative GEM, CFSv2 winds, or the MR model (cases A1, A2, and B1) were conducted. Additional cases include using the spatially uniform winds (i.e., the area-weighted average of the NNM data) and individually switching off winds, heat flux, river inputs, strait exchanges, and waves (cases C1–C6), respectively. It should be mentioned that wave effects were also excluded in case C2 since Lake Michigan is a pure wind-sea environment. Numerical runs with and without heat flux (cases A3 and C3) were carried out to understand the effects of wind and density-driven currents on lake surface circulation in the top sigma layer (i.e.,  $\frac{1}{40}$  of the local water depth).

To provide an in-depth analysis of the forcing mechanism of gyre circulation, monthly averaged simulations using the NNM winds scaled by 0.5, 0.75, and 1.25 (cases A4–A6) were added. One additional model run with a flat bottom (e.g., using the spatially uniform and flat bathymetry of the mean water depth at 85 m; case C7) was set to examine the bathymetric effects on the monthly gyre circulation. Hydrodynamic simulations were initialized on 2 April 2014 with a spatially uniform temperature of 4°C, and a salinity and current velocity of zero PSU and m/s, respectively. The model was spun up for 3 months before outputting the hydrodynamics over the period of July–September 2014. In addition to the monthly mean scale, effects of winds, heat flux, river inputs, strait exchanges, and waves on lake surface circulation in the top sigma layer at an episodic timescale were evaluated. The strong wind event lasts for 1 day (i.e., from 00:00 to 23:00 GMT on 11 September 2014), during which the mean and maximum speeds of the northerly winds are 10.4 and 14.4 m/s, respectively. A summary of the designed numerical experiments in 2014 is listed in Table 2. The validation experiment in the summer of 2015 follows the identical settings of the default run (case A3) in 2014.

#### 2.5. Skill Metrics

Statistical scores of the relative bias (*RB*), root-mean-square deviation (*RMSD*), and normalized Fourier norm (*F<sub>n</sub>*) (Schwab, 1983) were used to evaluate model's skill:

$$RB = (\overline{Model} - \overline{Obs}) / \overline{Obs} \quad (11)$$

$$RMSD = \left[ \frac{1}{N} \sum_{n=1}^N (Model_n - Obs_n)^2 \right]^{1/2} \quad (12)$$

**Table 1**

Locations, Depths, and Data Availability for Observed Wind Speed, Lake Surface Circulation (LSC), Lake Surface Temperature (LST), and Waves of Lake Michigan in the Summer of 2014

Variable	Station	Source	Availability	Lon. (°)	Lat. (°)	Depth (m)
Wind speed	45002	NDBC	1 July to 30 September	−86.411	45.344	175.3
	45007	NDBC	1 July to 30 September	−87.026	42.674	160
	MKGM4	GLERL	1 July to 30 September	−86.339	43.227	7.0
	45024	UM CILER	1 July to 30 September	−86.559	43.977	30.3
	MEEM4	NWS	1 July to 30 September	−86.346	44.248	8.6
LSC	Muskegon	ReCON	1 July to 12 September	−86.356	43.180	22.5
LST and wave parameter	45002	NDBC	1 July to 30 September	−86.411	45.344	175.3
	45007	NDBC	1 July to 30 September	−87.026	42.674	160
	45022	MTU	1 Jul. to 30 September	−85.088	45.403	49.1
	45024	UM CILER	1 July to 30 September	−86.559	43.977	30.3
	45161	GLERL	28 July to 12 August	−86.361	43.178	25
	45029	LT	1 July to 30 September	−86.272	42.900	27
	45026	LT	1 July to 30 September	−86.617	41.983	20.7
	45170	IISG & PCE	1 July to 30 September	−86.968	41.755	19.9
	45015	CPD	12 July to 28 August	−87.527	41.714	3.5
	45016	CPD	12 July to 5 August	−87.573	41.783	4.8
	45018	CPD	12 July to 2 September	−87.637	41.968	3.9
	C58W3	USCG	26 July to 30 September	−87.563	44.146	5.9
	0Y2W3	USCG	1 July to 30 September	−87.313	44.794	5.4
	45013	UWM	25 August to 30 September	−87.850	43.100	20.0
	SGNW3	NDBC	16 August to 30 September	−87.693	43.749	10.6
Wave parameter	45168	LT	31 July to 30 September	−86.331	42.397	20.4
	20CM4	USCG	10 July to 30 September	−86.490	42.090	5.8

Abbreviations: NDBC: National Data Buoy Center; GLERL: Great Lakes Environmental Research Laboratory; UM CILER: University of Michigan, Cooperative Institute for Great Lakes Research; NWS: National Weather Service; ReCON: Realtime Coastal Observations Network; MTU: Michigan Technology University; LT: Limno Tech; IISG & PCE: Illinois-Indiana Sea Grant & Purdue Civil Engineering; CPD: Chicago Park District; USCG: U.S. Coast Guard; UWM: University of Wisconsin-Milwaukee.

$$F_n = \left( \frac{1}{N} \sum_{n=1}^N |\vec{v}_o - \vec{v}_m|^2 \right)^{\frac{1}{2}} / \left( \frac{1}{N} \sum_{n=1}^N |\vec{v}_o|^2 \right)^{\frac{1}{2}} \quad (13)$$

where  $\overline{Model}$  and  $\overline{Obs}$  are the averaged values from the model ( $Model_n$ ) and observation ( $Obs_n$ ) in a sample of size  $N$ ;  $\vec{v}_m$  and  $\vec{v}_o$  are the modeled and observed current vectors;  $F_n$  stands for the relative variance unexplained by the model, of which the reasonable range is 0–1; a smaller value indicates a better skill (e.g., 0 means perfect estimation).

**Table 2**

Design of Numerical Experiments for the Summer of 2014 in Lake Michigan

Case name	Grid resolution	Wind input	Heat flux	River inputs	Strait exchanges	Wave effects	Bathy- metry
A1	HR	GEM	Yes	Yes	Yes	Yes	Real
A2	HR	CFSv2	Yes	Yes	Yes	Yes	Real
A3	HR	NNM	Yes	Yes	Yes	Yes	Real
A4	HR	0.5 × NNM	Yes	Yes	Yes	Yes	Real
A5	HR	0.75 × NNM	Yes	Yes	Yes	Yes	Real
A6	HR	1.25 × NNM	Yes	Yes	Yes	Yes	Real
B1	MR	NNM	Yes	Yes	Yes	Yes	Real
C1	HR	Uniform	Yes	Yes	Yes	Yes	Real
C2	HR	No	Yes	Yes	Yes	No	Real
C3	HR	NNM	No	Yes	Yes	Yes	Real
C4	HR	NNM	Yes	No	Yes	Yes	Real
C5	HR	NNM	Yes	Yes	No	Yes	Real
C6	HR	NNM	Yes	Yes	Yes	No	Real
C7	HR	NNM	Yes	Yes	Yes	Yes	Flat bottom



### 3. Results and Discussion

#### 3.1. Model Sensitivity Experiments

Numerical experiments first focused on the hydrodynamic responses to various wind sources and grid resolutions. Figure 2a shows time series of the surface current produced from the HR model forced by the GEM, CFSv2, and NNM winds (cases A1–A3) and that from the MR model (case B1) versus the ADCP measurement (Table 1 and Figure 1). The angle between the adjacent shoreline and east +x direction is 114°. Onshore and northward longshore currents are defined as positive, and vice versa. Observations indicated that the prevalent longshore current (e.g., between −25 and 34 cm/s) was stronger than the intermittent off-shore flow (e.g., between −5 and 13 cm/s). This phenomenon is consistent with the feature of coastal oceanography that cross-shelf flows are relatively weak compared to alongshore flows. Although Beletsky et al. (1999) found much smaller magnitudes of the mean current speed averaged over the summer (e.g., 0.1–4.5 cm/s), their observations supported our findings that the northward current was the dominant current pattern along the southeast shore. During the period of the highest observed current velocity around August 4, there was a phase shift in the simulated longshore current from case A3, presumably driven by the overly intensified NNM winds (e.g., up to 12 m/s) in the preceding days (Figure 2b). Given that the speeds of other two wind fields are lower (e.g., less than 9 m/s), the phase shift of currents relative to observations are less discernable. Compared to the observation-based data used previously (Beletsky et al., 2013), more buoys and meteorological stations (Jensen et al., 2012) were added to generate the NNM wind field in the current study. This improvement led to a better representation of the mesoscale winds by the NNM rather than the GEM or CFSv2, which consequently produced more accurate lake circulation.  $F_n$  for the wind vector at MKGM4 was 0.46 from the NNM data, while it was above 0.6 from the GEM or CFSv2. Consequently,  $F_n$  for the current vector from cases A1–A3 were 0.76, 0.84, and 0.67, and thus, the NNM wind was adopted to further examine the model's sensitivity to alternative grid resolutions.

Although  $F_n$  from the HR and MR models (0.67 and 0.68) were comparable, the more refined model showed better skill during the strong wind event on 3 August, which reduced the underestimated magnitude of longshore currents (34 cm/s) from 16 to 13 cm/s. The finding that the HR grid is significant to accurate simulations of coastal currents is supported by Niu et al. (2015) in Lake Erie. The scatterplot of surface temperature (Figure 3a) indicated that the HR model yielded smaller  $RB$  and  $RMSD$  averaged over all stations than those of the MR version (0.09°C and 2.61°C vs. 0.13°C and 3.08°C). The remaining model-to-data bias presumably originates from inaccurate model initializations (Beletsky et al., 2006), sigma coordinate-induced pressure gradient error (Haney, 1991; Mellor et al., 1994, 1998), or various tuning parameters in the hydrodynamic model (Beletsky & Schwab, 2001). By replacing the MR with HR grids, the model reduced the  $RMSD$  by less than 0.5°C in forecasting temperature fields for most locations. However, this treatment improved the  $RMSD$  by 0.78°C at the stations adjacent to the mid-west shore. Consequently, the monthly wind-driven upwelling and jet-like coastal currents along the mid-west shore in July of 2014 simulated by the HR model were 5 m/s greater than those from the MR model (section 3.3.3). This finding is consistent with Beletsky et al. (2006), which stated that increased model resolution (e.g., from 5 to 2 km) described the coastal dynamics better.

$F_n$  for the simulated surface current with various sigma layers were comparable in the range of 0.66–0.69 (not shown). However, the averaged  $RMSD$  for the surface temperature at 0–2 m depths below the water surface was largely improved from 2.73 to 2.61°C (i.e., 4.4% accuracy improvement with a  $p$  value below 0.05, meaning that the difference is statistically significant) by enhancing sigma layers from 5 to 20; this value decreased marginally to 2.59°C at 25 layers (not shown). The  $RMSD$  for surface temperature simulations over a seasonal timescale were at 1.3–1.6°C in mid-lake regions, which were comparable with those (e.g., 0.9–1.5°C) reported by Beletsky et al. (2006). Mellor et al. (1994) demonstrated that the calculated pressure gradient error was highly associated with sigma layer number, while this error-induced inaccuracy was insignificant when this number exceeded 20 (Niu et al., 2015). Given that the sigma layer was not orientated well with the horizontally uniform isopycnal, correcting the sigma layer-induced error like artificial thermal diffusion (Beletsky et al., 2006) by using a  $z$ -level model was a possible solution. However, the  $z$ -level coordinate has its own limitation that may introduce additional numerical errors near the bottom boundary layer (Ezer & Mellor, 2004). Because of this potential error, the  $z$ -level model was not used. When the sigma coordinate was replaced with the  $z$ -layering method to calculate the baroclinic pressure gradient, the  $RMSD$  for surface temperatures near the steep mid-west shore (e.g., slope of  $\sim 0.05$ ) were reduced (e.g., 3.16°C vs. 3.10°C),

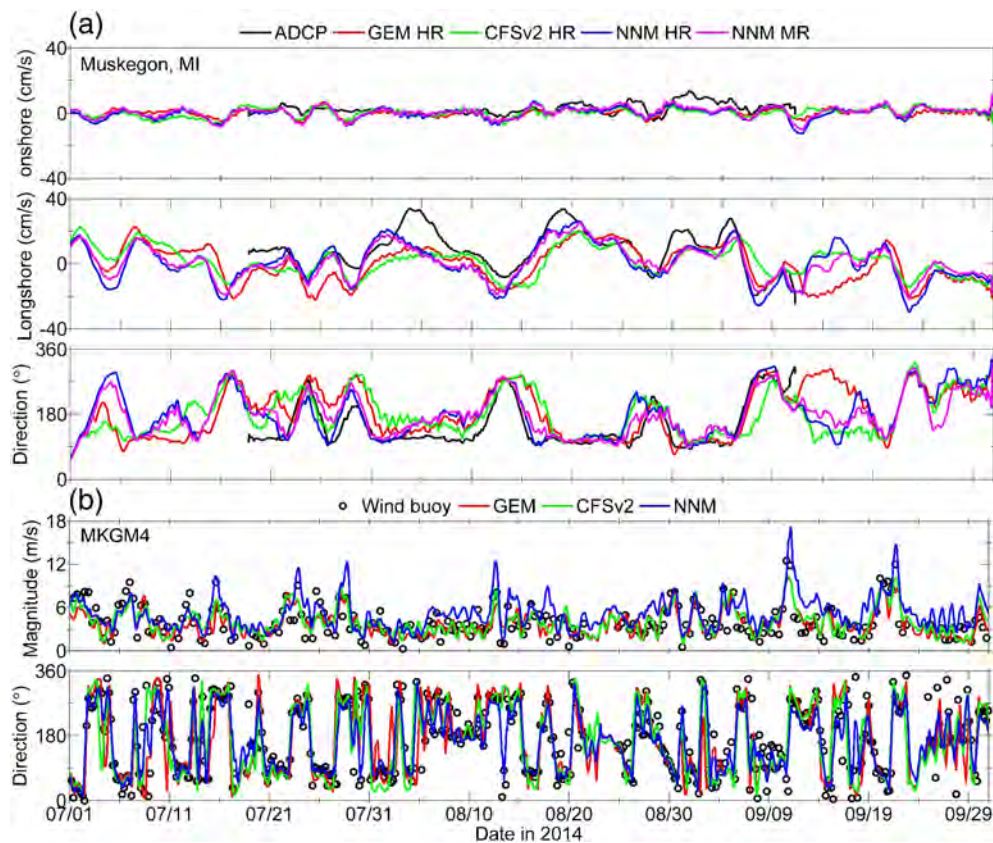


**Figure 2.** Time series of (a) onshore, longshore currents, and current directions from the HR model forced by three wind sources, and those from the MR model forced by the NNM winds versus ADCP measurement at Muskegon, in addition to (b) wind magnitude and direction from three wind sources versus buoy observations at MKGM4 from 1 July to 30 September 2014.

while they were increased (e.g.,  $3.21^{\circ}\text{C}$  vs.  $3.28^{\circ}\text{C}$ ) near the gentle southwest shore (e.g., slope of  $\sim 0.01$ ). By using the  $z$ -layering coordinate, lakes with relatively steeper bank gradients provide better baroclinic dynamics (e.g., surface temperatures) than sigma coordinates. Given that the ensemble-averaged  $RB$  and  $RMSD$  across all buoys for surface temperatures are identical between the sigma and  $z$ -layering methods, the sigma coordinates with 20 layers were adopted for this study.

After describing the model skill in simulating surface currents and temperature fields, the performance of the wave-current model in simulating waves was examined below. Despite a slight underestimation near the southern shore, modeled significant wave height (Figure 3b) scattered around the line of perfect agreement well in other regions, with the absolute  $RB$  and  $RMSD$  being less than or equal to 21% and 0.22 m. There is some bias in the wave model along the southeast shore and southern shore. Under the conditions of finite water depth with offshore winds, the significant wave heights are underpredicted (e.g.,  $RB$  of  $-0.19$  and  $-0.24$ , respectively) under the locally generated wind-wave conditions. It would be a worthwhile future endeavor to further improve the bore-based breaker model of Thornton and Guza (1983), such as using a joint scaling dependent method on local bottom slope and normalized wave number for the depth-induced wave breaking (Salmon et al., 2015; van der Westhuisen, 2010). Detailed calibration and validation of the wave model is referred to in Mao et al. (2016). After having selected the proper wind source and grid resolution (i.e., HR model with NNM winds), performance of the selected model (case A3) was validated in the next subsection.

### 3.2. Model Validation for Temperature and Current

To validate the model skill in hydrodynamic simulations, the monthly averaged lake surface temperatures simulated in the summer of 2015 were compared to those derived from the MODIS satellite imagery

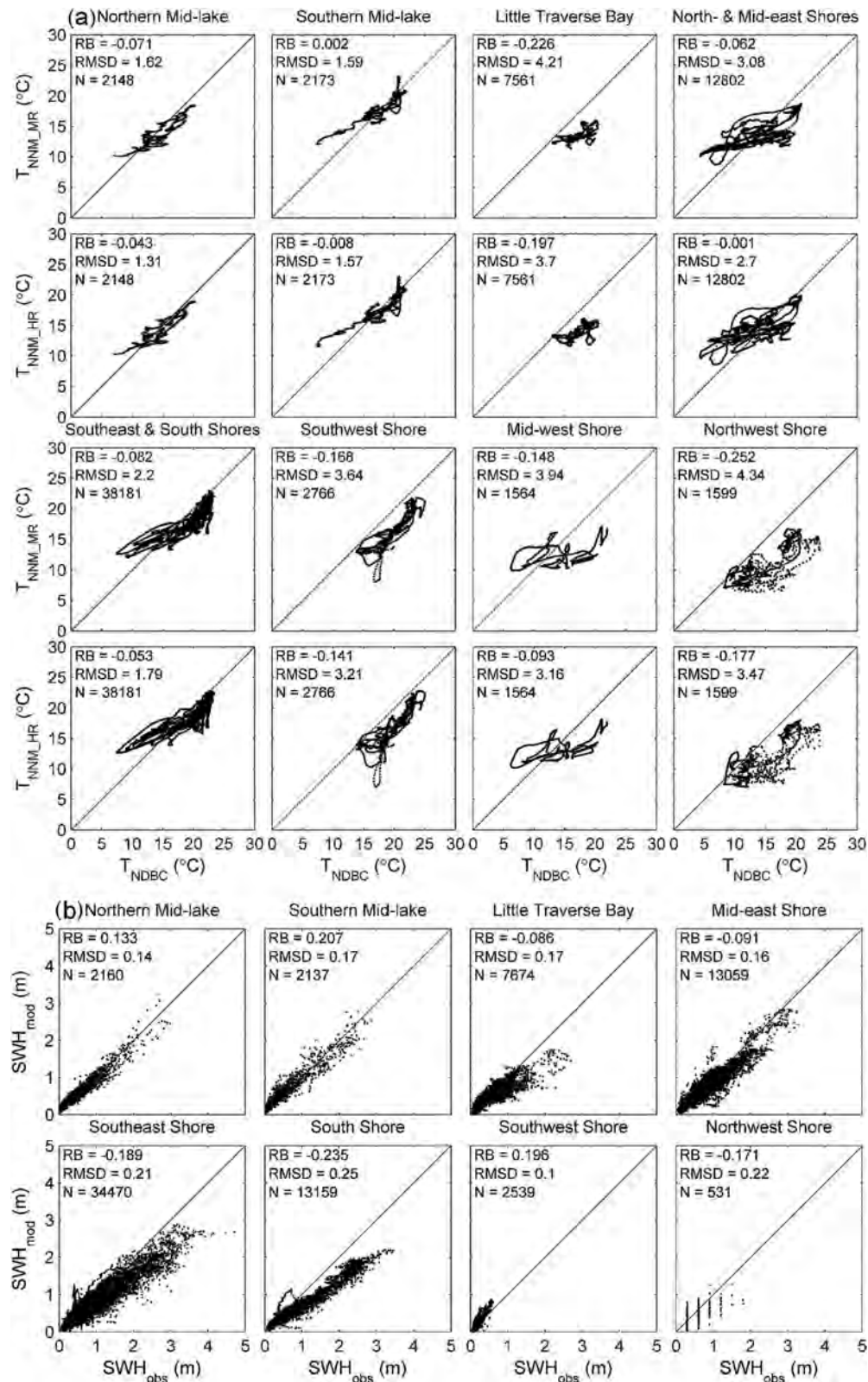


**Figure 3.** Scatterplot of (a) surface temperature produced from FVCOM with the NNM winds using the MR ( $T_{NNM\_MR}$ ) and HR ( $T_{NNM\_HR}$ ) grids versus observed values ( $T_{NDBC}$ ) taken at various NDBC buoys, and (b) SWH produced from SWAN ( $SWH_{mod}$ ) versus observations ( $SWH_{obs}$ ) at various NDBC stations from 1 July to 30 September 2014. SWH: significant wave height; N: number of samples.



(Figure 4a). The satellite images showed that the monthly averaged lake surface temperature (LST) over the entire lake followed a warming-cooling cycle from July to September (e.g., 19.9°C, 21.1°C, and 19.3°C), and this temporal trend was well captured by the simulations (e.g., 15.7°C, 17.7°C, and 16.8°C). This underestimation from the model can be explained by the fact that the MODIS data are taken from the lake's skin layer (e.g., the top few tens of micrometers of the water surface), while the simulated surface temperature in the numerical model are in the first sigma layer (e.g.,  $\frac{1}{40}$  of local water depths below the lake surface) during the warming summer. The spatial characteristics of LST observed from the satellite images (e.g., locally warming temperatures in the southern parts of Lake Michigan and Green Bay, and the relatively low temperature along the west shore) are well reproduced by the model. The ensemble-averaged *RMSD* for temperatures in the top sigma layer (e.g., less than 7 m below the water surface) was 3.8°C in this study, which was larger than that (e.g., 2.9°C in the upper 20 m) reported by Beletsky et al. (2006). Given that temperatures in the surface layer are more difficult to be simulated than those in the deeper layers (Beletsky et al., 2006), our model performance is acceptable for this application.

Model simulated currents were compared against observations at a shallow station 45013 (e.g., water depth of 20 m) near the mid-west shore (Figure 4b). Overall, the model reproduced the time series of the coastal current well (e.g., the ensemble mean of  $F_n$  from surface to bottom layers was 1.09). The observed longshore currents along the mid-west shore were stronger than the offshore component (e.g., up to 40 vs. <15 cm/s), which was well reflected by the simulation. Overall, both observations and model results suggest that the intensity of longshore currents decreased from surface to bottom layers.  $F_n$  for the near-bottom current vector from our simulation was 1.3, which was within the range of 0.92–1.59 predicted from Beletsky et al. (2006). Additionally, the finding that the near-surface current vector was more accurately predicted than the deeper one (e.g.,  $F_n = 0.52$  vs. 0.92–1.33) is consistent with that from Beletsky et al. (2006). These authors reported smaller values of  $F_n$  in the upper layers than the lower layers at several shallow and deep moorings (e.g., 0.96–1.09 vs. 0.99–1.1 at 20 m, 0.82–0.98 vs. 0.92–1.59 at 60 m, and 0.55 vs. 0.96 at 155 m). Compared to earlier predictions of current velocities in summer (e.g.,  $1 \leq F_n \leq 1.11$  in Allender, 1977;  $0.79 \leq F_n \leq 1.01$  in Schwab, 1983;  $0.95 \leq F_n \leq 1.05$  in Beletsky & Schwab, 2001;  $0.55 \leq F_n \leq 1.59$  in Beletsky et al., 2006), this study showed a comparable modeling skill in Lake Michigan ( $0.52 \leq F_n \leq 1.33$ ). It should be pointed out that the study from Beletsky et al. (2006) covered a large number of years (e.g., 1998–2003) and great number of current observations (e.g., seven moorings), while only two locations for 6 months in 2 years were included in this study.

Based on the model-to-data comparison over two summers using multiple observations (e.g., two ADCP stations for current velocities, satellite imagery for surface temperature fields, and various buoy stations for temperatures and significant wave heights), the validated model was further applied to investigate the monthly and episodic dynamics of summer circulation in the following subsection.

### 3.3. Dynamics of Lake Circulation

#### 3.3.1. Monthly Variability of Lake Hydrodynamics

Figure 5 depicts the monthly averaged NNM wind field and lake surface temperature (LST) from the baseline run (case A3), and the lake surface circulation (LSC) in the top sigma layer with (case A3) and without heat flux (case C3). The monthly averaged LST (Figures 5d1–5d3) showed variations from July to September with spatial means of 14.2°C, 17.3°C, and 15.7°C, respectively. In July, the upwelling-favorable, southwesterly winds (Figure 5a1) pumped up and transported the cold bottom water from the west shore to mid-lake, resulting in an appreciable, positive, offshore thermal gradient. The southeasterly winds near the east shore generated strong longshore currents in August (Figures 5a2 and 5b2), and the westerly winds near the west shore led to appreciable offshore flows extending from the jet-like longshore currents in September (Figures 5a3 and 5b3). From July to September, several mesoscale (e.g., 50- to 500-km length scale) cyclonic and anticyclonic (i.e., anticlockwise and clockwise) gyres were simulated (Figures 5b1–5b3). To highlight the monthly variability of lake surface circulation, spatial distributions of LSC and LST in the highly dynamic southern basin were further discussed below.

In July, a pair of current strips with a strong intensity up to 10–16 cm/s flowed northward along the southwest and mid-west shores (i.e., southwest current and mid-west current, hereafter referred to as SWC and MWC, see Figure 5b1). The SWC powered by a weak current from the south shore (4–8 cm/s) traversed



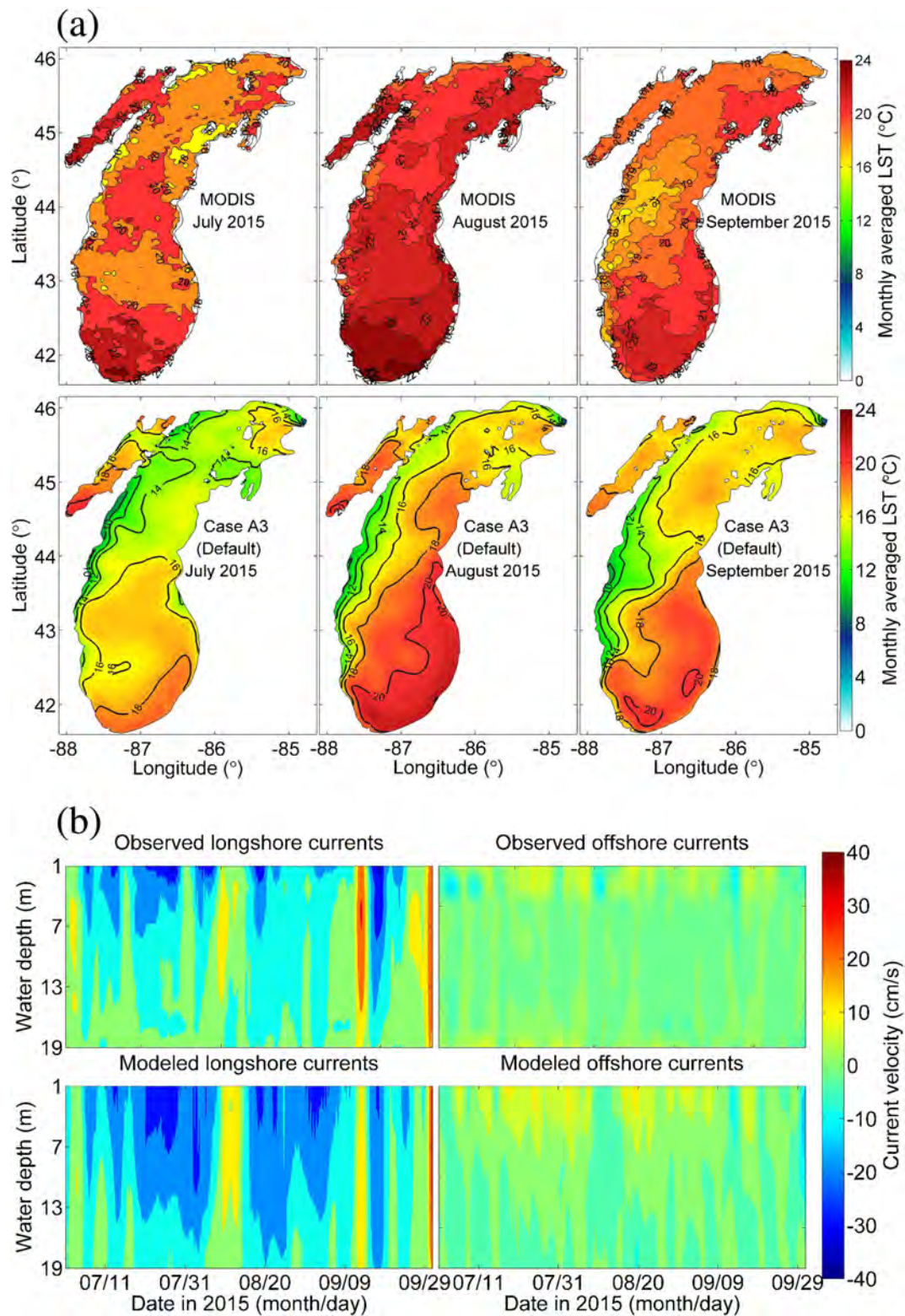


**Figure 4.** Model validation for the simulated (a) lake surface temperature (LST) against satellite imagery from MODIS and (b) current velocity against the ADCP observations at station 45013 in the summer of 2015; note: Positive values of longshore currents mean the adjacent mid-west shore is on the left of the flow direction.



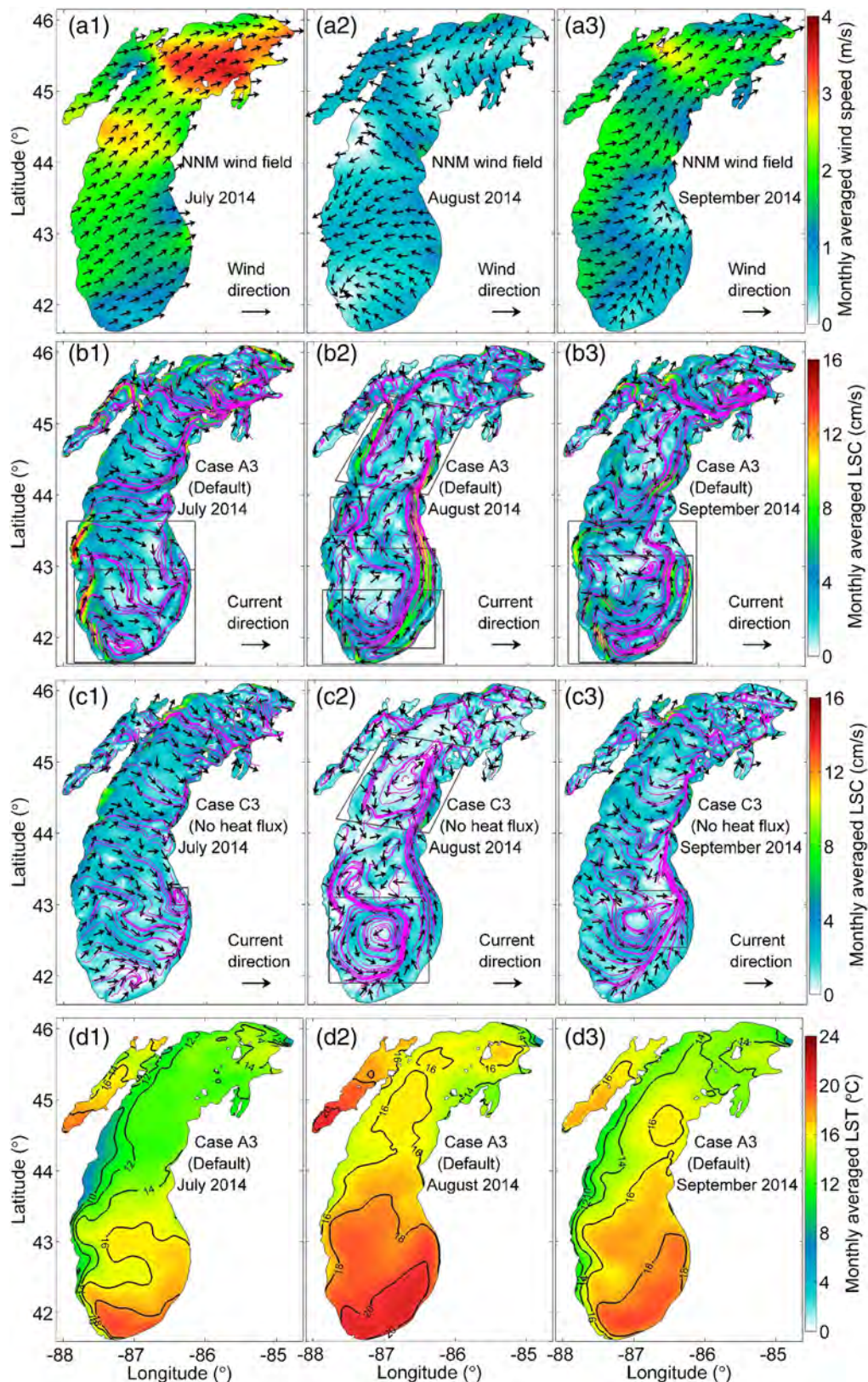


**Figure 5.** Monthly averaged (a1)–(a3) NNM winds, simulated LSC (b1)–(b3) with and (c1)–(c3) without heat flux; (d1)–(d3) are the simulated LST from the default case in the summer of 2014. Magenta lines and gray quadrilateral areas in (b1)–(c3) represent streamlines and major regions of gyre circulation.

the southern basin and connected to the feeding flow's tail near the east shore. Accordingly, a large anticyclonic gyre and semi-enclosed isotherms formed in proximity to the south shore. The MWC veered offshore before being split into two branches. The stronger portion (8–12 cm/s) traveled northeastward, whereas the other one moved across the mid-lake area and circulated along the south shore. Consequently, an immense anticyclonic gyre embraced the aforementioned one with a 2–3°C temperature difference. Comparing the directions between winds and surface currents (Figures 5a1 and 5b1), Ekman flows were more prevalent in the northern lake than its southern basin (e.g., surface flows moved at an angle of ~45° to the right of the wind overall), presumably attributed to distinct wind conditions over the northern and southern basins (e.g., wind speed of up to 4 vs. <2 m/s). The phenomenon that Ekman flows dominate surface circulation under strong wind conditions is consistent with previous findings in Georges Bank (Chen et al., 2003), the East China Sea (Chen et al., 2008), and the Gulf of Finland (Delpeche-Ellmann et al., 2016). These studies reported that the Ekman flow dominates coastal or ocean circulation under strong wind conditions, while it becomes less important under weak or calm conditions.

In August, three cyclonic gyres formed over Chippewa Basin, Mid-Lake Plateau, and South Chippewa Basin (Figure 5b2). In September, the lake circulation (Figure 5b3) was similar to that in July; the moderate variability of coastal currents in the southern lake between July and September was due to subtle changes of wind fields above the lake. Because of a weaker Ekman transport of the cold water from the west shore, the LST over South Chippewa Basin in September was higher than that in July.

### 3.3.2. Dominant Effects of Wind Forcing and Heat Flux on the Monthly Lake Dynamics

Summer circulation of Lake Michigan has significant monthly variations, which were dominated by density and wind-driven currents (Beletsky et al., 2006; Schwab & Beletsky, 2003). By excluding heat flux (case C3) from the baseline run (case A3), the strong coastal current generally became weaker (Figures 5c1–5c3). From case A3, the current intensities along the west shore in July and September and that along the east shore in August were up to 16, 12, and 14 cm/s, which were reduced by about half in case C3. Without the inclusion of heat flux, the paired anticyclonic gyres either disappeared or were replaced by a weaker cyclonic one. Moreover, the gyres over Chippewa Basin, Mid-Lake Plateau, and along the south shore vanished; the intensity of the gyre in South Chippewa Basin became half. From case A3 to C2 (i.e., no winds) and C3, the skill level of  $F_n$  for the current vector deteriorated from 0.67 to 1.08 and 0.80. For the LST from cases A3 to C2 and C3, the  $RB$  increased from 0.09 to 0.39 and 0.76, and the  $RMSD$  increased from 2.61 to 7.08 and 13.36°C, respectively.

To gain insights into the forcing mechanism of the paired anticyclonic gyres in southern Lake Michigan, the NNM winds scaled by 0.5, 0.75, and 1.25 and the spatially uniform winds (cases A4–A6 and C1) were used to drive the hydrodynamic model. Simulated monthly averaged LSC in July from various wind scenarios are shown in Figures 6a–6e. The increasing winds facilitated the gyre formation by reinforcing the coastal currents along the west shore (Figure 6c). By contrast, the reduced wind intensity led to the weakening of the current jet along the west shore (Figures 6a and 6b). In case A4, the consequent eastward transport crossing over the southern basin was destructed, and the characteristic gyres became less conspicuous and even disappeared. Although the basic gyre circulation in southern Lake Michigan still existed by using the spatially uniform wind field, intensities of the paired jets along the west shore were significantly reduced (Figure 6d). LSC changed dramatically by excluding the wind forcing (e.g., no gyre formation and quite weak coastal currents), which confirms the dominant impact of winds on the monthly gyre circulation.

Given the importance of local winds on coastal circulation, the gyre's signature is likely dependent upon wind direction, as demonstrated by previous simulations that various gyre patterns resulted from distinct wind conditions from July to September 2014 (Figures 5a1–5a3 and 5b1–5b3). However, the spatial linkage between the wind stress curl (Figure 6f) and gyre circulation (Figure 5b1) were quite weak or uncorrelated in South Chippewa Basin. In July, the wind stress curl ( $\frac{\partial \tau_y}{\partial x} - \frac{\partial \tau_x}{\partial y}$ ) in southern Lake Michigan was cyclonic at  $3.13 \times 10^{-9} \text{ N/m}^3$ , while the general circulation was anticyclonic. Schwab and Beletsky (2003) claimed that the baroclinicity was primarily responsible for the summer gyre circulation. In the current study, the significant influences of density-driven currents on the gyre circulation in South Chippewa Basin were supported by the distinct simulation results with and without heat flux (Figures 5b1 and 5c1). It can be concluded that wind-driven currents initiated the paired anticyclonic gyres near the shore (e.g., the dependence of gyre



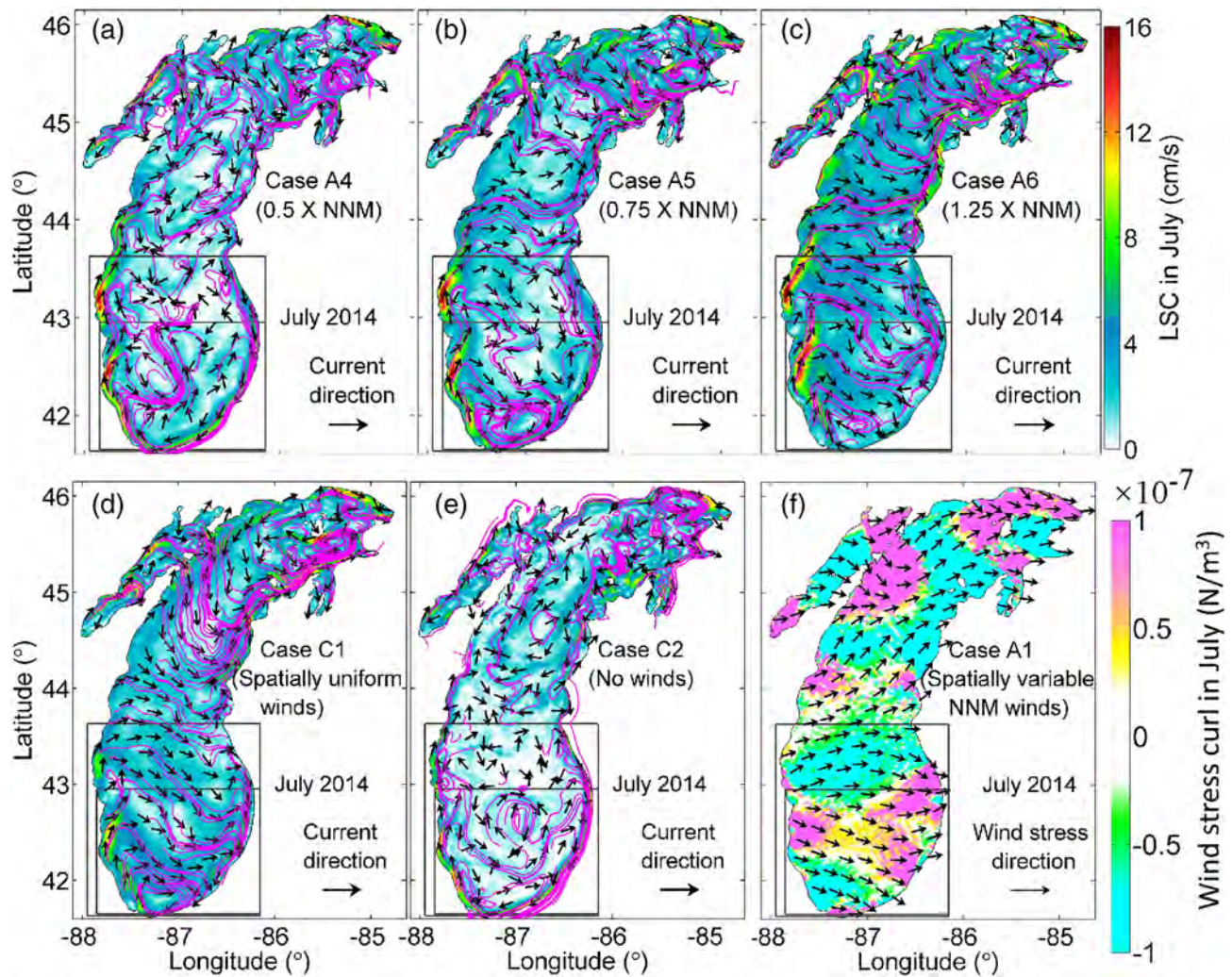


**Figure 6.** Monthly averaged (a)–(e) LSC in July 2014 from various wind scenarios and (f) wind stress curl calculated from the NNM winds. Black arrows in (a)–(e) and (f) represent current velocities and wind stresses. Magenta lines in (a)–(e) and gray quadrilateral areas in (a)–(f) represent streamlines and major regions of gyre circulation.

signature on winds), while their development in southern basin was strongly associated with the basin-scale density-driven flows.

### 3.3.3. Effects of External Forcing, Grid Resolution, and Bathymetry on the Monthly Lake Circulation

After having examined the dominating impacts of wind forcing and heat flux on the monthly averaged lake dynamics, Figures 7a–7e show the residual LSC in July from the default model (case A3) relative to that without river inputs, strait exchanges, waves, and that using the medium-resolution (MR) grid and flat bottom for model bathymetry (cases C4, C5, C6, B1, and C7), respectively. Effects of river inputs, strait exchanges, waves, and grid resolutions on the monthly LSC were quite weak and the gyre circulation pattern remained in southern Lake Michigan from cases C4, C5, C6, and B1 (not shown). Niu et al. (2015) reported that river-induced flows significantly impacted the water transport during spring in Lake Erie (e.g., up to 10 cm/s near Detroit River), while variability of the monthly circulation caused by river inputs in Lake Michigan was less than 1 cm/s near the river mouth. This phenomenon is not surprising considering the fact that the river discharge into Lake Erie (e.g., 5,300 and 5,700 m<sup>3</sup>/s from Detroit and Niagara Rivers) is over an order of magnitude larger than the total flows (404 m<sup>3</sup>/s) into Lake Michigan, while its lake size, depth, and volume are all much smaller compared to those of Lake Michigan.



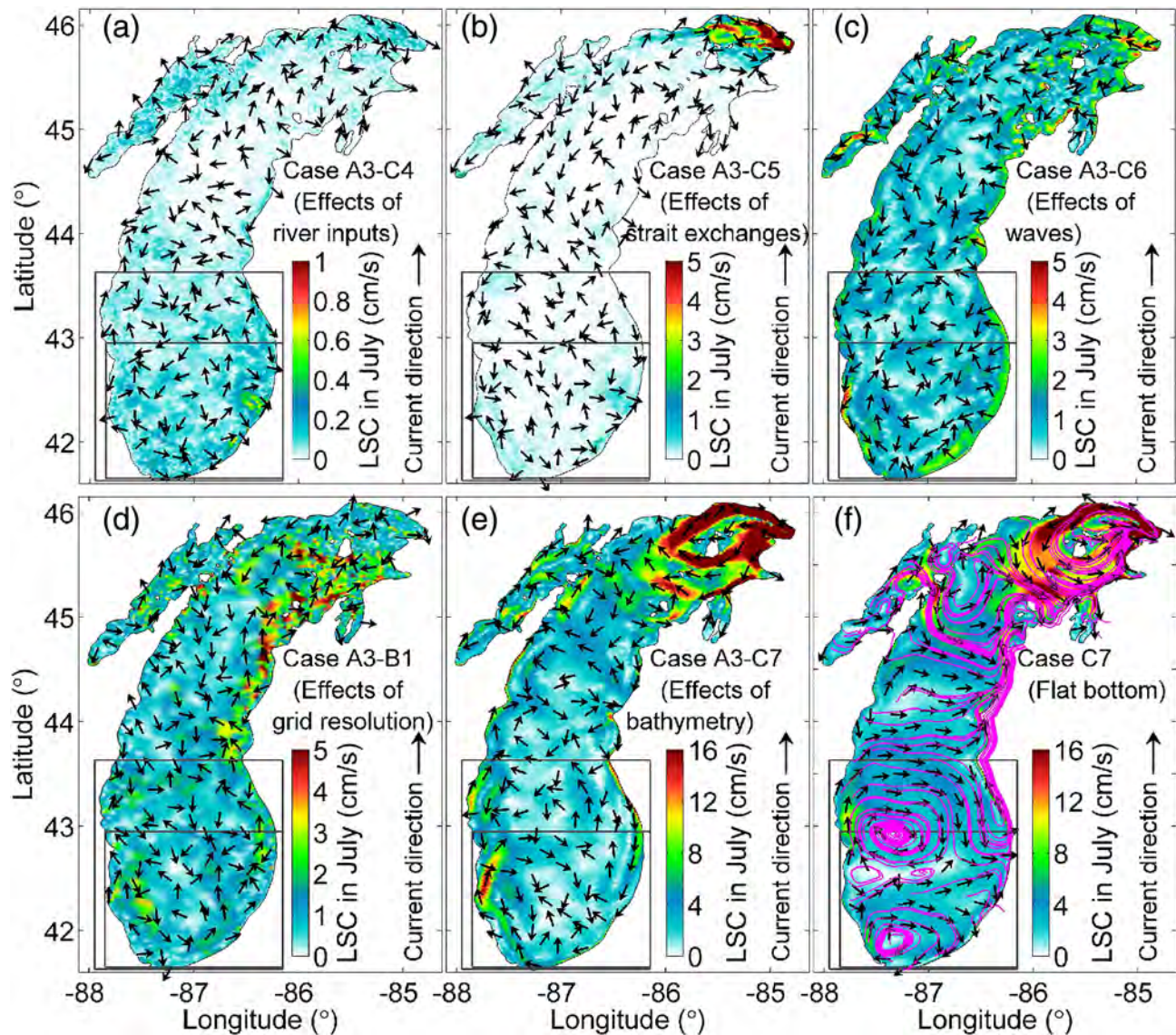


**Figure 7.** Residual LSC in July 2014 from the default model minus the one without (a) river inputs, (b) strait exchanges, (c) waves, and (d) that using the MR grids or (e) uniform bathymetry. Panel (f) is the LSC in July in the flat bottom case. Magenta lines in (f) and gray quadrilateral areas in (a)–(f) represent streamlines and major regions of gyre circulation.

Effect of strait exchanges on LSC was mainly limited within  $\sim 70$  km distance from Straits of Mackinac into Lake Michigan (e.g., up to 0.6 m/s), which is consistent with the finding from Anderson and Schwab (2013). Represented by the differences in mean surface current due to the presence of the straits during the period June–December 1990, Anderson and Schwab (2013) found that the area of influence near the straits extended up to 70 km northwestward into Lake Michigan. In most regions, opening the strait led to less than 1 cm/s variability of the current velocity (Figure 7b). By contrast, waves had a stronger impact on LSC and led to 1- to 2-cm/s variations of current velocity overall, especially in the nearshore region (2–5 cm/s, see Figure 7c). Along the southeast shore, wave-induced circulation was offshore directed, which tended to reduce the gyre size in southern Lake Michigan. Additionally, wave-induced southward longshore currents along the southwest shore decreased the jet intensity by 2–5 cm/s in the southern basin. The intensity of wave-induced circulation in this study was stronger than that ( $< 2$  cm/s) in Lake Erie (Niu & Xia, 2017), in which the mean value averaged over the entire water column was considered. Despite the inconsistency of the magnitude, both studies suggest that the wave-induced current is significant to lake circulation, and this process should be included in the hydrodynamic model.

Niu and Xia (2017) reported the mixing effect of wave-current interaction on the shallower Lake Erie, and it is interesting to examine how the wave coupling affects the surface mixed layer depth (MLD) in Lake Michigan. The criterion for the MLD is defined for the isopycnal or isothermal (e.g., no salinity variation) surface layers, and it is taken as the depth of the 0.8°C temperature difference from the surface layer (Kara et al., 2000). Figure 8 shows the MDL simulated from the model with and without wave effects (cases A3 and C6), in addition to their differences (case A3 minus C6) in the summer of 2014. The simulated monthly averaged MLD in the shallow region was in the range of 5–15 cm, which increased to 15–30 cm in the lake's northern and southern deep basins. As a result of the warming temperatures (e.g., enhancing thermal stratification) and reduced wind intensity in August (Figures 5a1–5a3 and 5d1–5d3), the MLD was shallower than those in July and September. Given that winds play an important role both in surface mixing and generating waves, the regions with larger MLD also experienced stronger wave effects. The wave coupling processes generally increased the MLD by 0–5 m, which even reached 15 m in parts of the northern basin. The spatially averaged MLD estimated from case C6 in July, August, and September were 10.6, 9.2, and 13.1 m, which were increased by 1.6, 0.6, and 2.3 m due to the wave coupling effects. During the strong wind event (Figures 8d1–8d4), the surface layer was more well mixed than that at a monthly timescale (e.g., MLD of 15–30 vs. 5–20 m). At an episodic timescale, the wave-induced alterations of MLD at most regions were between 5 and 15 m. Because the water column along the west shore and in the southern part of Green Bay had been well mixed during this strong wind event, the wave-induced variations of the MLD were less than 5 m in these shallow regions. Additional numerical runs by excluding one of the wave coupling processes individually (not shown here) suggests that the wave-altered sea surface roughness plays a dominant role in deepening the MLD at both the monthly and episodic timescales, while the wave-induced radiation stress and roller, wave-altered bottom stress, and Stokes drift are of secondary importance. This finding is consistent with the previous study in Lake Erie (Niu & Xia, 2017), which stated that wave-altered sea surface roughness is primarily responsible for the effects of waves on lake temperatures and thermal structures (e.g., through the enhanced mixing effect and the accelerated air-lake heat flux).

Beletsky et al. (2006) suggested that a model with refined grids is critical to reproduce the wind-driven upwelling and subsequent anticyclonic gyres. To examine whether a high-resolution (HR) model is necessary to resolve both the coastal current and gyre circulation, simulations produced by the MR model (case B1) are included for a comparison (Figure 7d). By replacing the HR model with the MR one, variations of current velocity were 2–3 cm/s along the southwest shore, which increased to 3–5 cm/s near the east shore, particularly in the shallow area at north of the lake. Moreover, the HR model produced stronger coastal jets along the west shore and better facilitated the gyre circulation in southern Lake Michigan. This result is consistent with a previous finding from Beletsky et al. (2006), which stated that a higher-resolution grid is key to resolve the wind-driven upwelling along the lake's west shore.

The simulated paired anticyclonic gyres are attributed to the great ability of the HR model in resolving the highly variable coastal bathymetry (e.g., the convex shoreline between the paired jets) and multiscale lake dynamics. From the perspective of physical oceanography, formation of the paired gyres derives from the wind-induced, jet-like, Ekman currents along the west shore and the density-driven circulation in South Chippewa Basin. In addition to the basin-scale circulation, the HR model reproduced nearshore currents well at the length scale of baroclinic Rossby radius (3–5 km) within the coastal boundary layer (8–10 km). By refining grid resolutions from 5 to 2 km, Beletsky et al. (2006) improved coastal modeling and simulated one anticyclonic gyre in southern Lake Michigan. The significance of grid resolution in modeling gyre circulation is supported by researches in the Gulf of Mexico (Romanou et al., 2004), Lake Superior (Bennington et al., 2010), and Lake Erie (Niu et al., 2015).

The MR model simulated the general pattern of lake circulation, and the HR version produced stronger upwelling processes and jet-like currents along the mid-west (e.g., 12–14 vs. 14–16 cm/s) and southwest shores (e.g., 8 vs. 12–14 cm/s). Computational times consumed in modeling the lake circulation with the MR and HR grids (e.g., a cold start on 2 April and an end on 1 October 2014) are 195 and 584 core hours. As meshes continue to grow in number (e.g., from 9,581 to 38,324 elements), simulations were conducted in the parallel system (e.g., 72 processors in the Computational & Information Systems Lab Cheyenne high-performance computer clusters), which required 8.1 and 2.7 hr by using the HR and MR models for one case. Considering the improvement of using a higher-resolution model in modeling the temperature



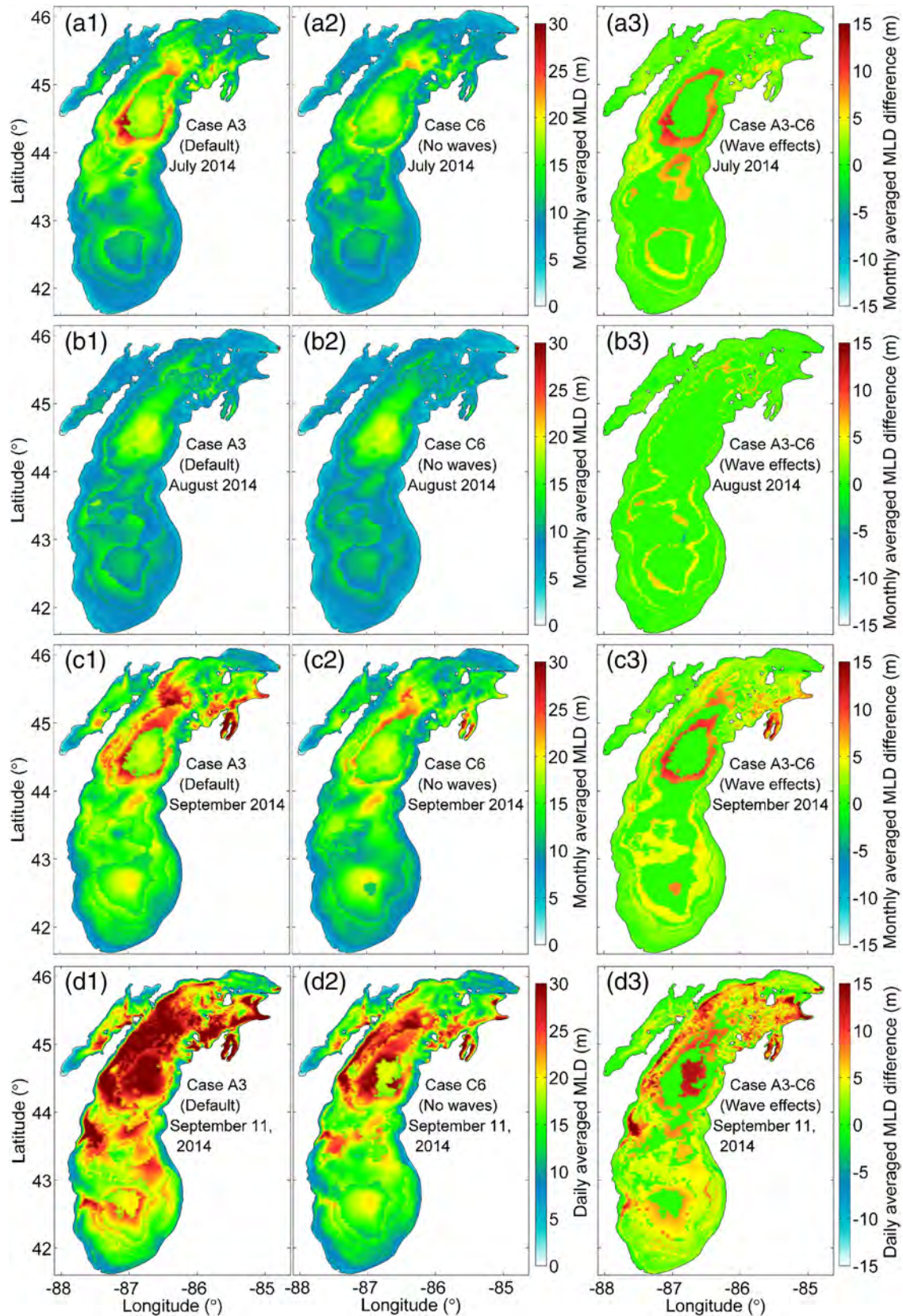


**Figure 8.** Mixed layer depth (MLD) in (a1)–(a3) July, (b1)–(b3) August, (c1)–(c3) September, and (d1)–(d3) during the strong wind event in 2014; left, middle, and right columns are MLD simulated from the model with and without waves, in addition to their differences.

fields and the rapid development of the computer power, it is feasible to apply the HR model for this study. A further refined grid may slightly improve the accuracy but will likely be achieved at an overly expensive cost (e.g., reducing both the grid size and corresponding model time step to half will cost  $16 \times 8.1 = 130$  hr computation times per case). Given that the baroclinic Rossby radius of Lake Michigan in summer is on the order of 5 km (Beletsky et al., 2006), using grid sizes less than 5 km is critical for resolving the upwelling processes along the mid-west shore (e.g., 1.1–1.5 km in our study and 2 km in Beletsky et al., 2006) in the future development of similar models.

To further examine the factors that influence the monthly gyres sitting roughly in the two primary basins of the lake, one additional model run (case C7) with a hypothetically flat bottom (e.g., using the spatially uniform water depth of 85 m) was conducted. Effects of lake bathymetry on gyre circulation (Figure 7f) were generally greater than those from river inputs, strait exchanges, waves, and grid resolutions (e.g., up to 16 vs. 5 cm/s, see Figure 7). By artificially setting the lake bathymetry as a flat bottom, the model produced Ekman-style surface flows in the northern basin, similar to the result from the standard run (case A3). In addition, case C7 simulated double anticyclonic gyres in the southern basin (Figure 7f). Compared to case A3, the simulated magnitude of jet-like currents along the west shore by using the uniform bathymetry was relatively small (e.g., less than 12 cm/s), and the paired gyres were tangent to each other externally. It can be concluded that effects of lake bathymetry are not as significant as those from winds and heat flux, but they are still important to the gyre circulation in the lake's southern basin. The conclusion that bathymetric effects are profound to circulation patterns is consistent with previous studies in Lake Michigan (Schwab & Beletsky, 2003) and other lakes in the Great Lakes system (Beletsky et al., 2012; Bennington et al., 2010).

#### **3.3.4. Persistence of Monthly Lake Circulation Pattern**

To study whether the circulation patterns are persistent across multiple years, spatial distributions of the monthly averaged wind speeds and surface current velocities in the summer of 2015 are depicted in Figure 9. The wind field in July 2015 resembled that of July 2014 (e.g., southwesterly dominated and an increased intensity following the longitudinal axis northwardly), resulting in a similar pattern of lake surface currents, such as westerly flows in the northern basin and anticyclonic gyre circulation in the southern lake. Given that the coastal currents along the northwest shore from 43.5°N to 44.5°N became stronger in 2015 (e.g., increased from 4 to 12 cm/s), the gyre size was larger than that simulated in 2014. Because the wind field adjacent to the southern shore in August 2015 was larger than that of August 2014 (e.g., 2 vs. 1 m/s), the simulated magnitude of the anticyclonic gyre in this region was enhanced from 8 to 12 cm/s.

The spatial wind distribution in September 2015 (e.g., southerly dominated) showed a distinct pattern than that of September 2014; thus, the model simulated a small anticyclonic gyre confined to a narrow zone off the southwest shore in 2015. However, the larger anticyclonic gyres remained in the southern basin, presumably due to the similar thermal structures (e.g., responsible for the baroclinic currents) between 2 years (e.g., Figures 4a and 5d3). The finding that the anticyclonic gyre is often located in the southern basin and that its size, shape, and strength vary across multiple years are consistent with the previous modeling and observational results of summer circulation during 1998–2003 (Beletsky et al., 2006). By comparing the monthly averaged LSC to the surface wind and temperature fields, it can be concluded that the inter-annual variability of gyre dynamics in Lake Michigan (e.g., mainly found in the southern basin) is dominated by the atmospheric forcing (e.g., wind and density-driven currents). This conclusion is consistent with previous findings in Lake Superior during 1976–2006 (Bennington et al., 2010) and Lake Erie during 1995–1996 and 2002–2008 (Niu et al., 2015).

#### **3.3.5. Dynamics of Lake Circulation During a Strong Wind Event**

Strong wind events generate large waves, high surges, and strong currents (Mao et al., 2016; Mao & Xia, 2017), and thus, present several physical hazards to the coastal community. This section discussed dynamics of lake circulation during a strong wind event, which lasted for 1 day from 00:00 to 23:00 GMT on 11 September 2014. Figures 10a–10c show spatial patterns of wind speed, significant wave height, and lake surface circulation during this episodic event. In the middle lake, magnitude of the northeasterly, Ekman-driven, surface currents reached ~20 cm/s. Along the northwest shore, speed of wind-induced, surface, longshore currents was up to 80 cm/s, which was much larger than that in the nearshore region of Lake Erie (<40 cm/s) (Niu & Xia, 2017). In Lake Erie, current velocity is averaged across the entire water column, which likely results in a compromised intensity in the surface layer.



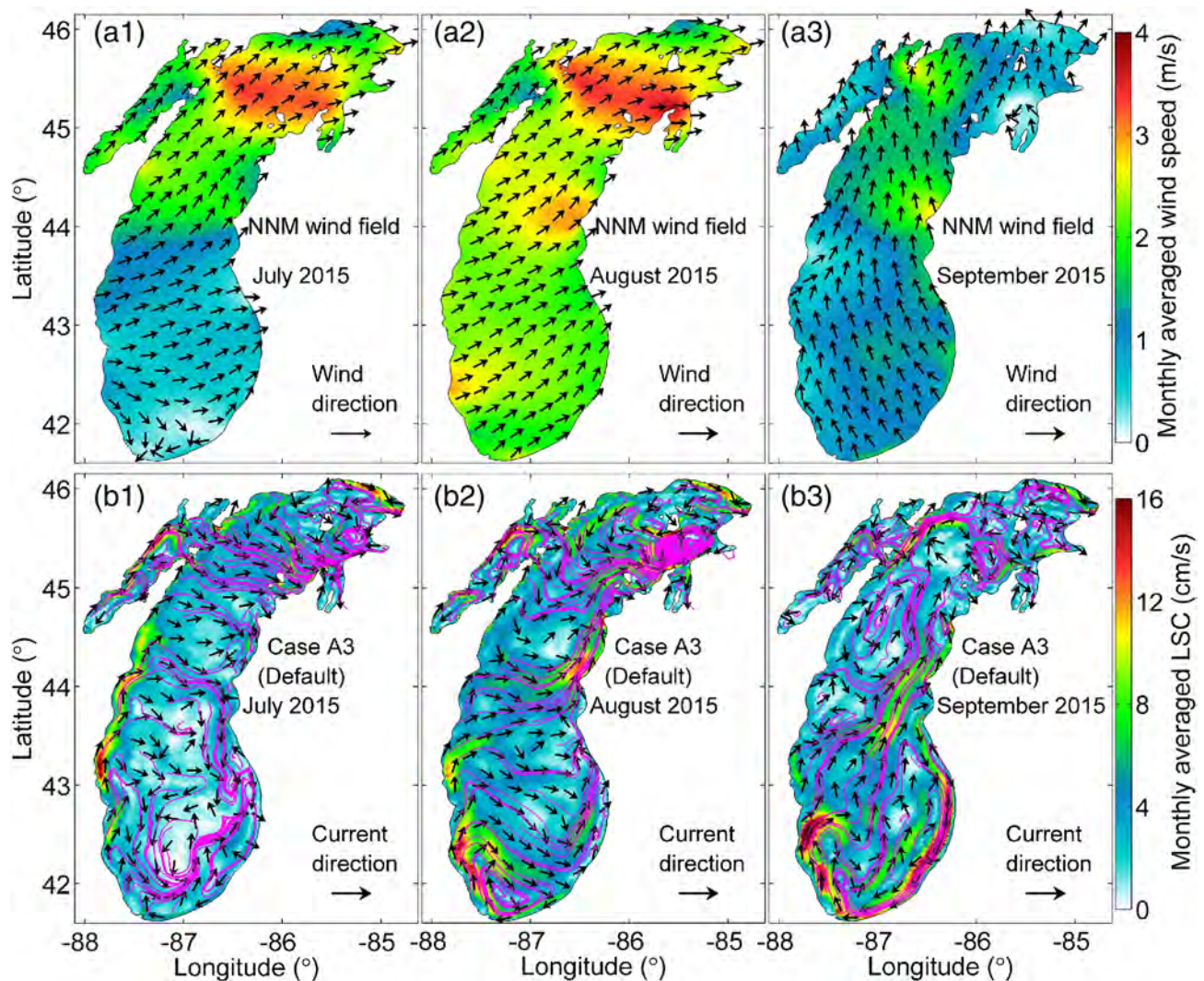


**Figure 9.** Monthly averaged (a1)–(a3) NNM winds and (b1)–(b3) simulated LSC in the summer of 2015. Magenta lines in (b1)–(b3) represent streamlines.

At an episodic timescale, wind and density-driven currents dominated lake surface circulation (e.g., up to 80 and 20 cm/s, respectively), while effects of river inputs, strait exchanges, waves, and grid resolution are of secondary importance (Figures 10d–10i). Although wind and density-induced currents in the mid-lake (10–20 cm/s) were comparable, the former one was predominant in coastal regions (e.g., up to 80 vs. <10 cm/s). As expected, river-induced flows marginally influenced lake surface circulation (<5 cm/s), and strait exchanges mainly impacted the region adjacent to Straits of Mackinac. As a result of strait exchanges, current variations reached 10 cm/s in southern Green Bay. This phenomenon is likely due to a large amount of water flowing into Green Bay from northern Lake Michigan (Mao & Xia, 2017). By replacing the MR grid with the HR one, the area of influence for current velocities during this episodic event was similar to that at a monthly timescale in July, but the magnitude of current variations became triple (e.g., 0–15 vs. 0–5 cm/s, see Figures 7d and 10i).

Wave-induced circulation was mostly discernable in the shallow Green Bay and lake's nearshore (Figure 10h). Wave-driven flows are highly irregular in Green Bay, attributed to the complex wind-wave-current-bathymetry interaction (e.g., depth-induced breaking and bottom friction). Wave-induced longshore currents near the lake's southwest and southeast shores reached 15 cm/s, likely caused by the wave-breaking-induced radiation stress (Niu & Xia, 2017). During this northerly wind event, waves up to 2-m significant wave height prevailed over the southern basin (Figure 10b) and experienced strong depth-induced breaking



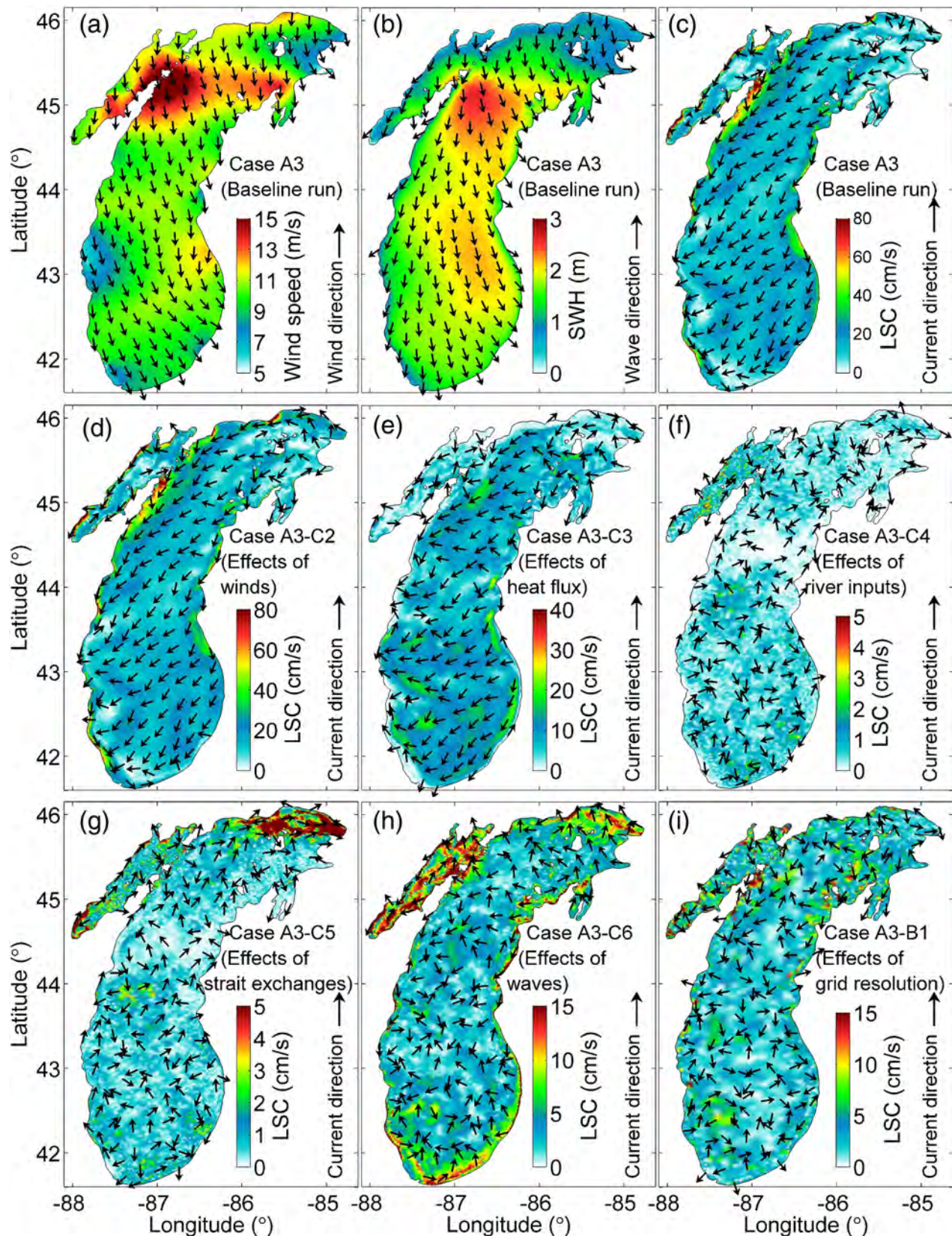


**Figure 10.** Spatial distributions of (a) wind speed, (b) significant wave height (SWH), (c) LSC from the baseline run, and residual LSC caused by (d) winds, (e) heat flux, (f) river inputs, (g) strait exchanges, (h) waves, and (i) lower-resolution grids during a strong wind event on 11 September 2014.

approaching the south shore (Mao et al., 2016). Wave-induced longshore currents (0.05–0.15 m/s) are comparable to those in Lake Erie during a storm event (e.g., up to 0.2 m/s) (Niu & Xia, 2017), but smaller than those during a hurricane event in Maryland Coastal Bays (e.g., up to 1.5 m/s) (Mao & Xia, 2018). However, both studies (Mao & Xia, 2018; Niu & Xia, 2017) support the finding that wave radiation stress is a primary contribution to the wave-induced longshore currents in the nearshore. Meanwhile, onshore waves led to offshore currents up to 15 cm/s along the lake's south shore, which was represented as the complementary flow for the wave-induced Stokes drift (Lentz & Fewings, 2012). Overall, wave-induced circulation is important to coastal circulation during a strong wind event, and this process was incorporated into the numerical model in this study.

### 3.3.6. Vertical Inhomogeneity of Lake Circulation

To investigate vertical distributions of lake circulation, depth-averaged, middle, and bottom (e.g., 10th and 20th sigma layers at  $\frac{19}{40}$  and  $\frac{39}{40}$  of the local water depth) current fields from the baseline run (case A3) at both monthly and episodic timescales were examined (Figure 11). Given the complexity and its ecological importance, lake circulation in southern Lake Michigan was discussed in detail. In July, double anticyclonic gyres simulated in the surface layer still existed in the middle and bottom layers, while intensities of current jets reduced to 8 and 2 cm/s, respectively (Figures 11a2 and 11a3). Consequently, coastal jets originating from the west shore disappeared in the bottom layer. In August, the externally tangent, surface gyre circulation was present in the middle and bottom layers (Figures 11b2 and 11b3). In the middle/bottom layer, the current intensity along the eastern perimeter of the cyclonic gyre became weaker than that of the surface layer (4–8/0–2 vs. 8–12 cm/s). In September, cyclonic and anticyclonic gyres developed in the middle and bottom layers (Figures 11c2 and 11c3). The different gyre patterns between surface and middle/bottom layers are related to the reduced wind impacts on the underlying basin-scale circulation (Delpêche-Ellmann et al., 2016). During the strong wind event, the circulation in the middle layer was quite similar to that in the surface, especially in the shallow nearshore (Figures 10c and 11d2). In the middle deep-water regions, waters in the middle and bottom layers flowed in an opposite direction relative to that in the surface layer (e.g., southwesterly versus northeasterly, see Figures 10c and 11d3) due to the enclosed nature of the lake's land boundary (Mao & Xia, 2017; McCombs et al., 2014). The vertical inhomogeneity during the stratified period is supported by observations from Choi et al. (2012), which indicated that the observed currents decreased with depths from the surface to bottom in southern Lake Michigan during 1998–1999. The direct measurement data in the Western Central mooring sites of Lake Superior supported the vertical inhomogeneity as lake stratified, which observed strong currents over the top 20 m and weak opposing ones below that during summer 2010 (Austin, 2013). The vertical inhomogeneity of lake circulation suggests that an accurate representation of the complex three-dimensional circulation is key to understanding plume dynamics and fish larval spreading in Lake Michigan (Beletsky et al., 2017; Chen et al., 2004).

## 4. Conclusions

This study investigated the monthly and episodic dynamics of the 2014 summer circulation in Lake Michigan by using a high-resolution, three-dimensional (3D), wave-current coupled finite-volume community ocean model (FVCOM). Numerical simulations with three wind field sources and two grid resolutions were compared against observations in the summer of 2014. Model performance was well validated with additional data from satellite imagery (e.g., surface temperature fields) and the nearshore mooring (e.g., current profiles) in the summer of 2015. Relative contributions of various forces, grid resolutions, and bathymetry to lake dynamics and gyre circulation have been given a detailed discussion, and main conclusions are summarized as follows:

1. The high-resolution, wave-current coupled model driven by the observation-based NNM wind data provides better skill in simulating coastal currents than that using the GEM and CFSv2 wind products (e.g., the normalized Fourier norm  $F_n$  of 0.67 vs. 0.76 and 0.84), likely because the NNM wind field agrees strongly with the NDBC buoy-recorded data. This sensitivity study would be of interest to modelers using FVCOM and similar ocean models in the Great Lakes system, including the Princeton Ocean Model (Beletsky et al., 2006; Blumberg & Mellor, 1987).
2. Compared to previous works in coastal simulations, this study shows comparable modeling skill for the Eulerian current velocity (0.55–1.59 vs. 0.52–1.33 for  $F_n$ ). It should be pointed out that the previous works



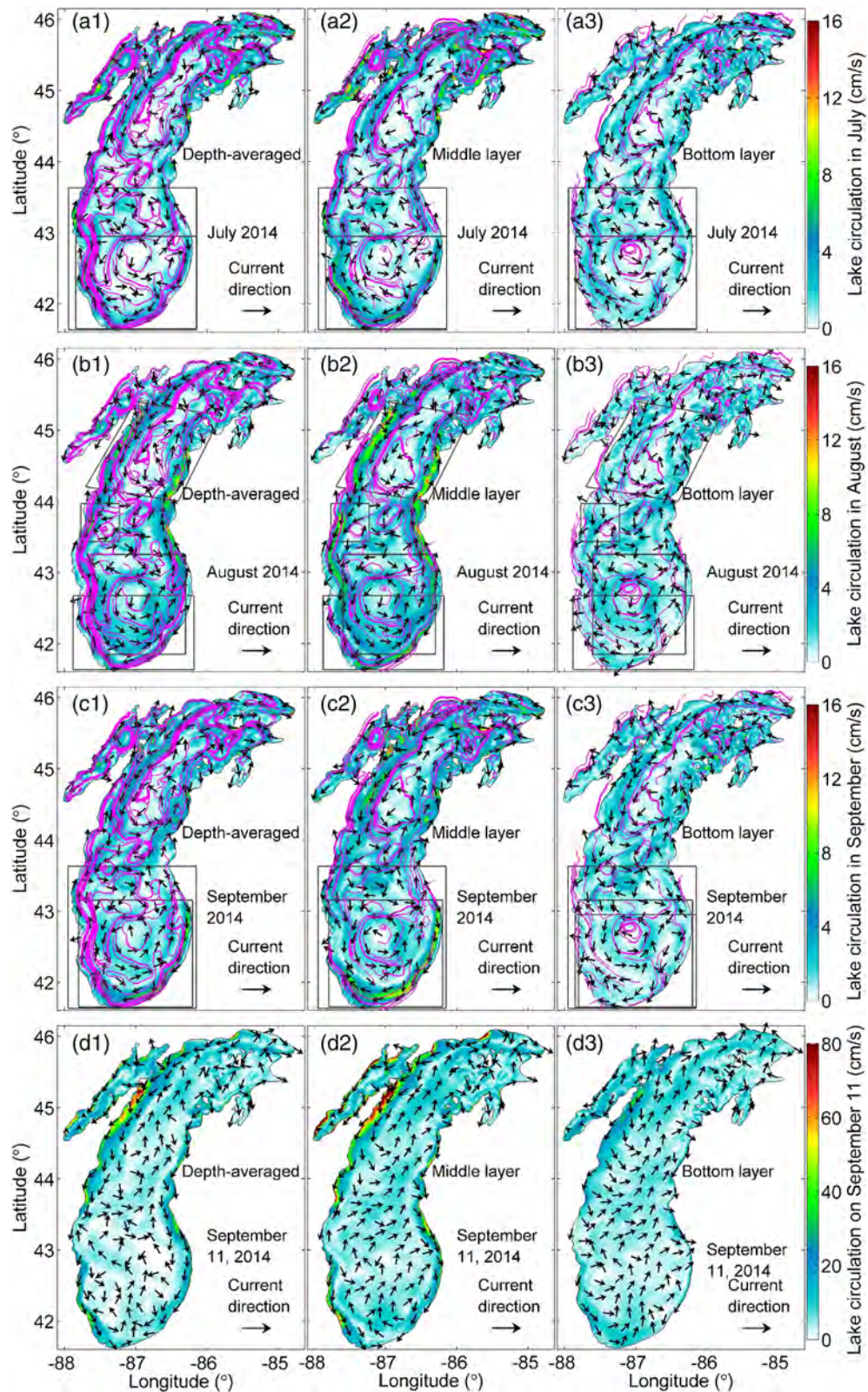


**Figure 11.** Lake circulation in (a1)–(a3) July, (b1)–(b3) August, (c1)–(c3) September, and (d1)–(d3) during the strong wind event in 2014; left, middle, and right columns are depth-averaged currents, and those in the middle and bottom layers. Magenta lines and gray quadrilateral areas in (a1)–(c3) represent streamlines and major regions of gyre circulation.



(Beletsky et al., 2006) covered a large number of years (e.g., 1998–2003) and great number of current observations (e.g., seven moorings), while only two locations for 6 months in 2 years were considered for this study. Beletsky et al. (2006) reported a root-mean-square error for surface temperatures at mid-lake stations of 0.9–1.5°C, the value reported herein was comparable at 1.3–1.6°C. Supplemental observations from surface drifters (Harrington, 1894; Liu et al., 1976) and Eulerian moorings covering a wider spatial space of the lake would be a worthwhile future endeavor. Given the highly sensitive dependence of drifter tracks on initial conditions (e.g., two similar flow fields can result in dramatically different drifter tracks), a statistical representation of surface drifter tracks (e.g., ensemble mean) might be helpful.

3. Analysis of model sensitivity results indicates that wind and density-driven currents dominate monthly lake surface circulation in the top sigma layer (e.g., coastal current and gyre pattern), while it is also influenced by river inputs (<1 cm/s), strait exchanges (<1 cm/s except for the nearby region), waves, (<5 cm/s) grid resolution (<5 cm/s), and bathymetry (<16 cm/s). Numerical results obtained during a strong wind event (>10 m/s) support the predominant impacts of wind and density-driven currents (e.g., up to 80 and 20 cm/s, respectively) on lake surface circulation in the top sigma layer at an episodic timescale.
4. In July 2014, a pair of anticyclonic gyres, with current jets along the west shore (12–16 cm/s), was simulated in southern Lake Michigan. The paired anticyclone gyres are attributed to the ability of the numerical model in resolving the multiscale bathymetry and lake dynamics (e.g., the intense coastal current jet at 3–5 km length scale, Rossby radius within the 8–10 km coastal boundary layer, and basin-scale circulation). Numerical simulations suggest that the forcing mechanism of the paired anticyclonic gyres is the wind-driven, upwelling-favorable, jet-like, Ekman currents along the western coast, connected by the density-driven, basin-scale circulation in the deep southern basin. Vertical inhomogeneity of the simulated horizontal currents suggests that further investigation of the complex 3D lake circulation and their effects on ecological issues is a worthwhile future endeavor.

The work conducted in this study will be useful for other large lakes in the Great Lakes system, such as Lake Superior and Lake Huron. The offline wave coupling to the circulation model FVCOM would not be specific to SWAN, other wind-wave models (e.g., WAVEWATCH III) (Alves et al., 2014) that are capable of producing the wave variable data (including the significant wave height, peak wave period, mean wave direction, mean wavelength, bottom wave orbital velocity, and period) can also be potentially used in this offline coupling method.

## Data Availability Statement

The water surface elevation data were retrieved from NOS (<https://tidesandcurrents.noaa.gov/stationhome.html?id=9075080>), the bathymetry data of Lake Michigan were freely available at the NGDC (<http://www.ngdc.noaa.gov/mgg/greatlakes/greatlake.html>), and the ADCP data at Muskegon station were generated by Mr. S. Ruberg and distributed by the GLERL's ReCON (<http://www.glerl.noaa.gov/res/recon/data/2014/mich-mkg>). The NASA's Aqua MODIS satellite image data is available online (<https://modis.gsfc.nasa.gov>). Model results are archived and can be freely accessed at Open Science Framework (<https://osf.io/khy6z/>).

## Acknowledgments

This project was supported by a National Science Foundation grant to M. Xia (1238044), and also NOAA GLERL. Dr. D.J. Schwab is greatly appreciated for his constructive discussion with Xia on the wave-current coupled model and nearshore dynamics, and comments from Dr. D. Beletsky on gyre circulation are highly appreciated. Dr. S.J. Lentz hosted Xia's short visit to the Woods Hole Oceanographic Institution and provided insightful comments on the wave-current dynamics. The authors greatly appreciated four anonymous reviewers and the Editor for their constructive comments that significantly improve the quality of this manuscript. Numerical experiments were conducted on the CISL's Yellowstone and Cheyenne, and Stampede's HPC machines from the Texas Advanced Computing Center.

## References

- Allender, J. H. (1977). Comparison of model and observed currents in Lake Michigan. *Journal of Physical Oceanography*, 7(5), 711–718. [https://doi.org/10.1175/1520-0485\(1977\)007%3C;0711:COMAOC%3E;2.0.CO;2](https://doi.org/10.1175/1520-0485(1977)007%3C;0711:COMAOC%3E;2.0.CO;2)
- Alves, J. H. G., Chawla, A., Tolman, H. L., Schwab, D. J., Lang, G., & Mann, G. (2014). The operational implementation of a Great Lakes forecasting system at NOAA/NCEP. *Weather and Forecasting*, 29(6), 1473–1497. <https://doi.org/10.1175/WAF-D-12-00049.1>
- Anderson, E. J., & Schwab, D. J. (2013). Predicting the oscillating bi-directional exchange flow in the Straits of Mackinac. *Journal of Great Lakes Research*, 39(4), 663–671. <https://doi.org/10.1016/j.jglr.2013.09.001>
- Anderson, E. J., & Schwab, D. J. (2017). Meteorological influence on summertime baroclinic exchange in the Straits of Mackinac. *Journal of Geophysical Research*, 122, 2171–2182. <https://doi.org/10.1002/2016JC012255>
- Ardhuin, F., Hamon, M., Collard, F., Chapron, B., & Queffelecoul, P. (2008). Spectral wave evolution and spectral dissipation based on observations: A global validation of new source functions. In: Proceedings, 4<sup>th</sup> Chinese–German Joint Symposium on Coastal and Ocean Engineering, Darmstadt, Germany.
- Austin, J. (2013). Observations of near-inertial energy in Lake Superior. *Limnology and Oceanography*, 58(2), 715–728. <https://doi.org/10.4319/lo.2013.58.2.0715>

- Bai, X., Wang, J., Schwab, D. J., Yang, Y., Luo, L., Leshkevich, G. A., & Liu, S. (2013). Modeling 1993–2008 climatology of seasonal general circulation and thermal structure in the Great Lakes using FVCOM. *Ocean Modelling*, 65, 40–63. <https://doi.org/10.1016/j.ocemod.2013.02.003>
- Beletsky, D., Beletsky, R., Rutherford, E. S., Sieracki, J. L., Bossenbroek, J. M., Chadderton, W. L., et al. (2017). Predicting spread of aquatic invasive species by lake currents. *Journal of Great Lakes Research*, 43(3), 14–32. <https://doi.org/10.1016/j.jglr.2017.02.001>
- Beletsky, D., Hawley, N., & Rao, Y. R. (2013). Modeling summer circulation and thermal structure of Lake Erie. *Journal of Geophysical Research: Oceans*, 118, 6238–6252. <https://doi.org/10.1002/2013JC008854>
- Beletsky, D., Hawley, N., Rao, Y. R., Vanderploeg, H. A., Beletsky, R., Schwab, D. J., & Ruberg, S. A. (2012). Summer thermal structure and anticyclonic circulation of Lake Erie. *Geophysical Research Letters*, 39, L06605. <https://doi.org/10.1029/2012GL051002>
- Beletsky, D., O'Connor, W. P., Schwab, D. J., & Dietrich, D. E. (1997). Numerical simulation of internal Kelvin waves and coastal upwelling fronts. *Journal of Physical Oceanography*, 27(7), 1197–1215. [https://doi.org/10.1175/1520-0485\(1997\)027%3C;1197:NSOIKW%3E;2.0.CO;2](https://doi.org/10.1175/1520-0485(1997)027%3C;1197:NSOIKW%3E;2.0.CO;2)
- Beletsky, D., Saylor, J. H., & Schwab, D. J. (1999). Mean circulation in the Great Lakes. *Journal of Great Lakes Research*, 25(1), 78–93. [https://doi.org/10.1016/S0380-1330\(99\)70718-5](https://doi.org/10.1016/S0380-1330(99)70718-5)
- Beletsky, D., & Schwab, D. J. (2001). Modeling circulation and thermal structure in Lake Michigan: Annual cycle and interannual variability. *Journal of Geophysical Research*, 106(C9), 19,745–19,771. <https://doi.org/10.1029/2000JC000691>
- Beletsky, D., & Schwab, D. J. (2008). Climatological circulation in Lake Michigan. *Geophysical Research Letters*, 35, L21604. <https://doi.org/10.1029/2008GL035773>
- Beletsky, D., Schwab, D. J., & McCormick, M. J. (2006). Modeling the 1998–2003 summer circulation and thermal structure in Lake Michigan. *Journal of Geophysical Research*, 111, C10010. <https://doi.org/10.1029/2005JC003222>
- Beletsky, D., Schwab, D. J., Roebber, P. J., McCormick, M. J., Miller, G. S., & Saylor, J. H. (2003). Modeling wind-driven circulation during the March 1998 sediment resuspension event in Lake Michigan. *Journal of Geophysical Research*, 108(C2), 3038. <https://doi.org/10.1029/2001JC001159>
- Bennington, V., McKinley, G. A., Kimura, N., & Wu, C. H. (2010). General circulation of Lake Superior: Mean, variability, and trends from 1979 to 2006. *Journal of Geophysical Research*, 115, C12015. <https://doi.org/10.1029/2010JC006261>
- Blumberg, A. F., & Mellor, G. L. (1987). A description of a three-dimensional coastal ocean circulation model. In N. S. Heaps (Ed.), *Three-dimensional coastal ocean models, Coastal and Estuarine Sciences Series* (Vol. 4, pp. 1–16). Washington, D.C.: AGU. <https://doi.org/10.1029/CO004p0001>
- Bolaños, R., Brown, J. M., & Souza, A. J. (2014). Wave–current interactions in a tide dominated estuary. *Continental Shelf Research*, 87, 109–123. <https://doi.org/10.1016/j.csr.2014.05.009>
- Chen, C., Beardsley, R. C., Cowles, G., Qi, J., Lai, Z., Gao, G., et al. (2013). An unstructured grid, finite-volume community ocean model FVCOM user manual, third Ed., *SMAS/UMASSD Tech. Rep.-13-0701*, pp. 404, Univ. of Mass.-Dartmouth, New Bedford, Massachusetts.
- Chen, C., Schlitz, R. J., Lough, R. G., Smith, K. W., Beardsley, R. C., & Manning, J. P. (2003). Wind-induced, cross-frontal exchange on Georges Bank: A mechanism for early summer on-bank biological particle transport. *Journal of Geophysical Research*, 108(C11), 8011. <https://doi.org/10.1029/2002JC001358>
- Chen, C., Wang, L., Ji, R., Budd, J. W., Schwab, D. J., Beletsky, D., et al. (2004). Impacts of suspended sediment on the ecosystem in Lake Michigan: A comparison between the 1998 and 1999 plume events. *Journal of Geophysical Research*, 109, C10S05. <https://doi.org/10.1029/2002JC001687>
- Chen, C., Xue, P., Ding, P., Beardsley, R. C., Xu, Q., Mao, X., et al. (2008). Physical mechanisms for the offshore detachment of the Changjiang diluted water in the East China Sea. *Journal of Geophysical Research*, 113, C02002. <https://doi.org/10.1029/2006JC003994>
- Chen, C., Zhu, J., Ralph, E., Green, S. A., Budd, J. W., & Zhang, F. Y. (2001). Prognostic modeling studies of the Keweenaw current in Lake Superior. Part I: Formation and evolution. *Journal of Physical Oceanography*, 31(2), 379–395. [https://doi.org/10.1175/1520-0485\(2001\)031%3C;0379:PMSOTK%3E;2.0.CO;2](https://doi.org/10.1175/1520-0485(2001)031%3C;0379:PMSOTK%3E;2.0.CO;2)
- Choi, J., Hsieh, T.-C., Hawley, N., & McCormick, M. J. (2012). A year of internal Poincaré wave in southern Lake Michigan. *Journal of Geophysical Research*, 117, C07014. <https://doi.org/10.1029/2012JC007984>
- Côté, J., Gravel, S., Méthot, A., Patoine, A., Roch, M., & Staniforth, A. (1998). The operational CMC-MRB global environmental multiscale (GEM) model. Part I: Design considerations and formulation. *Monthly Weather Review*, 126(6), 1373–1395. [https://doi.org/10.1175/1520-0493\(1998\)126%3C;1373:TOCMGE%3E;2.0.CO;2](https://doi.org/10.1175/1520-0493(1998)126%3C;1373:TOCMGE%3E;2.0.CO;2)
- Delpeche-Ellmann, N., Torsvik, T., & Soomere, T. (2016). A comparison of the motions of surface drifters with offshore wind properties in the Gulf of Finland, the Baltic Sea. *Estuarine, Coastal and Shelf Science*, 172, 154–164. <https://doi.org/10.1016/j.ecss.2016.02.009>
- Donelan, M. A., Dobson, F. W., Smith, S. D., & Anderson, R. J. (1993). On the dependence of sea surface roughness on wave development. *Journal of Physical Oceanography*, 23(9), 2143–2149. [https://doi.org/10.1175/1520-0485\(1993\)023%3C;2143:OTDOSS%3E;2.0.CO;2](https://doi.org/10.1175/1520-0485(1993)023%3C;2143:OTDOSS%3E;2.0.CO;2)
- Ezer, T., & Mellor, G. L. (2004). A generalized coordinate ocean model and a comparison of the bottom boundary layer dynamics in terrain-following and in z-level grids. *Ocean Modelling*, 6(3–4), 379–403. [https://doi.org/10.1016/S1463-5003\(03\)00026-X](https://doi.org/10.1016/S1463-5003(03)00026-X)
- Fairall, C. W., Bradley, E. F., Rogers, D. P., Edson, J. B., & Young, G. S. (1996). Bulk parameterization of air-sea fluxes for tropical ocean-global atmosphere coupled-ocean atmosphere response experiment. *Journal of Geophysical Research*, 101(C2), 3747–3764. <https://doi.org/10.1029/95JC03205>
- Galperin, B., Kantha, L. H., Hassid, S., & Rosati, A. (1988). A quasi-equilibrium turbulent energy model for geophysical flows. *Journal of the Atmospheric Sciences*, 45(1), 55–62. [https://doi.org/10.1175/1520-0469\(1988\)045%3C;0055:AQETEM%3E;2.0.CO;2](https://doi.org/10.1175/1520-0469(1988)045%3C;0055:AQETEM%3E;2.0.CO;2)
- Haney, R. L. (1991). On the pressure gradient force over steep topography in sigma coordinate ocean models. *Journal of Physical Oceanography*, 21(4), 610–619. [https://doi.org/10.1175/1520-0485\(1991\)021%3C;0610:OTPGFO%3E;2.0.CO;2](https://doi.org/10.1175/1520-0485(1991)021%3C;0610:OTPGFO%3E;2.0.CO;2)
- Harrington, M. W. (1894). *Currents of the Great Lakes: As deduced from the movements of bottle papers during the seasons of 1892 and 1893*. Washington, D.C.: U.S. Weather Bureau.
- Janssen, P. A. E. M. (1991). Quasi-linear theory of wind-wave generation applied to wave forecasting. *Journal of Physical Oceanography*, 21(11), 1631–1642. [https://doi.org/10.1175/1520-0485\(1991\)021%3C;1631:QLTOWW%3E;2.0.CO;2](https://doi.org/10.1175/1520-0485(1991)021%3C;1631:QLTOWW%3E;2.0.CO;2)
- Jensen, R. E., Cialone, M. A., Chapman, R. S., Ebersole, B. A., Anderson, M., & Thomas, L. (2012). Lake Michigan storm: Wave and water level modeling. *Tech. Rep. ERDC/CHL-TR-12-26*, Coastal and Hydraul. Lab., U.S. Army Eng. Res. and Dev. Cent. Vicksburg, Miss.
- Kara, A. B., Rochford, P. A., & Hurlburt, H. E. (2000). Mixed layer depth variability and barrier layer formation over the North Pacific Ocean. *Journal of Geophysical Research*, 105(C7), 16,783–16,801. <https://doi.org/10.1029/2000JC900071>
- Lang, G. A., & Leshkevich, G. A. (2014). Persistent wind fields over the Great Lakes, 2002–2013. Paper presented at 57th Annual Conference on Great Lakes Research, McMaster Univ., Hamilton, Ontario, Canada, 26–30, May.
- Large, W. G., & Pond, S. (1981). Open ocean momentum flux measurements in moderate to strong winds. *Journal of Physical Oceanography*, 11(3), 324–336. [https://doi.org/10.1175/1520-0485\(1981\)011%3C;0324:OOMFMI%3E;2.0.CO;2](https://doi.org/10.1175/1520-0485(1981)011%3C;0324:OOMFMI%3E;2.0.CO;2)

- Lentz, S. J., & Fewings, M. R. (2012). The wind- and wave-driven inner-shelf circulation. *Annual Review of Marine Science*, 4(1), 317–343. <https://doi.org/10.1146/annurev-marine-120709-142745>
- Liu, P. C., Miller, G. S., & Saylor, J. H. (1976). Water motion. In *Limnology of lakes and embayments*, (pp. 119–149). Great Lakes Basin Framework Study. Appendix 4). Ann Arbor, Michigan: Great Lakes Basin Commission.
- Madsen, O. S. (1994). Spectral wave-current bottom boundary layer flows. In *Coastal Engineering 1994, Proceedings of the 24th International Conference, Coastal Engineering Research Council* (pp. 384–398). Kobe, Japan: American Society of Civil Engineers.
- Mao, M., van der Westhuysen, A. J., Xia, M., Schwab, D. J., & Chawla, A. (2016). Modeling wind waves from deep to shallow waters in Lake Michigan using unstructured SWAN. *Journal of Geophysical Research: Oceans*, 121, 3836–3865. <https://doi.org/10.1002/2015JC011340>
- Mao, M., & Xia, M. (2017). Dynamics of wave–current–surge interactions in Lake Michigan: A model comparison. *Ocean Modelling*, 110, 1–20. <https://doi.org/10.1016/j.ocemod.2016.12.007>
- Mao, M., & Xia, M. (2018). Wave–current dynamics and interactions near the two inlets of a shallow lagoon–inlet–coastal ocean system under hurricane condition. *Ocean Modelling*, 129, 124–144. <https://doi.org/10.1016/j.ocemod.2018.08.002>
- McCombs, M. P., Mulligan, R. P., Boegman, L., & Rao, Y. R. (2014). Modeling surface waves and wind-driven circulation in eastern Lake Ontario during winter storms. *Journal of Great Lakes Research*, 40, 130–142. <https://doi.org/10.1016/j.jglr.2014.02.009>
- Mellor, G. L. (2003). The three-dimensional current and surface wave equations. *Journal of Physical Oceanography*, 33(9), 1978–1989. [https://doi.org/10.1175/1520-0485\(2003\)033%3C;1978:TTCASW%3E;2.0.CO;2](https://doi.org/10.1175/1520-0485(2003)033%3C;1978:TTCASW%3E;2.0.CO;2)
- Mellor, G. L. (2008). The depth-dependent current and wave action equations: A revision. *Journal of Physical Oceanography*, 38(11), 2587–2596. <https://doi.org/10.1175/2008JPO3971.1>
- Mellor, G. L. (2015). A combined derivation of the integrated and vertically resolved, coupled wave–current equations. *Journal of Physical Oceanography*, 45(6), 1453–1463. <https://doi.org/10.1175/JPO-D-14-0112.1>
- Mellor, G. L., Ezer, T., & Oey, L.-Y. (1994). The pressure gradient conundrum of sigma coordinate ocean models. *Journal of Atmospheric and Oceanic Technology*, 11(4), 1126–1134. [https://doi.org/10.1175/1520-0426\(1994\)011%3C;1126:TPGCOS%3E;2.0.CO;2](https://doi.org/10.1175/1520-0426(1994)011%3C;1126:TPGCOS%3E;2.0.CO;2)
- Mellor, G. L., Oey, L.-Y., & Ezer, T. (1998). Sigma coordinate pressure gradient errors and the seamount problem. *Journal of Atmospheric and Oceanic Technology*, 15(5), 1122–1131. [https://doi.org/10.1175/1520-0426\(1998\)015%3C;1122:SCPGA%3E;2.0.CO;2](https://doi.org/10.1175/1520-0426(1998)015%3C;1122:SCPGA%3E;2.0.CO;2)
- Murthy, C. R., & Dunbar, D. S. (1981). Structure of the flow within the coastal boundary layer of the Great Lakes. *Journal of Physical Oceanography*, 11(11), 1567–1577. [https://doi.org/10.1175/1520-0485\(1981\)011%3C;1567:SOTFWT%3E;2.0.CO;2](https://doi.org/10.1175/1520-0485(1981)011%3C;1567:SOTFWT%3E;2.0.CO;2)
- Niu, Q., & Xia, M. (2017). The role of wave–current interaction in Lake Erie's seasonal and episodic dynamics. *Journal of Geophysical Research: Oceans*, 122, 7291–7311. <https://doi.org/10.1002/2017JC012934>
- Niu, Q., Xia, M., Ludsins, S. A., Chu, P. Y., Mason, D. M., & Rutherford, E. S. (2018). High-turbidity events in western Lake Erie during ice-free cycles: Contributions of river-loaded versus resuspended sediments. *Limnology and Oceanography*, 63(6), 2545–2562. <https://doi.org/10.1002/lno.10959>
- Niu, Q., Xia, M., Rutherford, E. S., Mason, D. M., Anderson, E. J., & Schwab, D. J. (2015). Investigation of interbasin exchange and inter-annual variability in Lake Erie using an unstructured-grid hydrodynamic model. *Journal of Geophysical Research: Oceans*, 120, 2212–2232. <https://doi.org/10.1002/2014JC010457>
- Olabarrieta, M., Warner, J. C., & Kumar, N. (2011). Wave-current interaction in Willapa Bay. *Journal of Geophysical Research*, 116, C12014. <https://doi.org/10.1029/2011JC007387>
- Phillips, O. M. (1977). The dynamics of surface waves. *The dynamics of the upper ocean* (2nd ed., pp. 33–98). Cambridge, U. K.: Cambridge Univ. Press.
- Podsetchine, V., & Schernewski, G. (1999). The influence of spatial wind homogeneity on flow patterns in a small lake. *Water Research*, 33(15), 3348–3356. [https://doi.org/10.1016/S0043-1354\(99\)00035-4](https://doi.org/10.1016/S0043-1354(99)00035-4)
- Qi, J., Chen, C., Beardsley, R. C., Perrie, W., Cowles, G. W., & Lai, Z. (2009). An unstructured-grid finite-volume surface wave model (FVCOM-SWAVE): Implementation, validations and applications. *Ocean Modelling*, 28(1–3), 153–166. <https://doi.org/10.1016/j.ocemod.2009.01.007>
- Rao, D. B., & Murty, T. S. (1970). Calculation of the steady state wind-driven circulation in Lake Ontario. *Archiv für Meteorologie, Geophysik und Bioklimatologie, Serie A*, 19(2), 195–210. <https://doi.org/10.1007/BF02249005>
- Rao, Y. R., & Schwab, D. J. (2007). Transport and mixing between the coastal and offshore waters in the Great Lakes: A review. *Journal of Great Lakes Research*, 33(1), 202–218. [https://doi.org/10.3394/0380-1330\(2007\)33\[202:TAMBTC\]2.0.CO;2](https://doi.org/10.3394/0380-1330(2007)33[202:TAMBTC]2.0.CO;2)
- Rogers, W. E., Hwang, P. A., & Wang, D. W. (2003). Investigation of wave growth and decay in the SWAN model: Three regional-scale applications. *Journal of Physical Oceanography*, 33(2), 366–389. [https://doi.org/10.1175/1520-0485\(2003\)033%3C;0366:IOGWAD%3E;2.0.CO;2](https://doi.org/10.1175/1520-0485(2003)033%3C;0366:IOGWAD%3E;2.0.CO;2)
- Romanou, A., Chassignet, E. P., & Sturges, W. (2004). Gulf of Mexico circulation within a high-resolution numerical simulation of the North Atlantic Ocean. *Journal of Geophysical Research*, 109, C01003. <https://doi.org/10.1029/2003JC001770>
- Rowe, M. D., Anderson, E. J., Vanderploeg, H. A., Pothoven, S. A., Elgin, A. K., Wang, J., & Yousef, F. (2017). Influence of invasive quagga mussels, phosphorus loads, and climate on spatial and temporal patterns of productivity in Lake Michigan: A biophysical modeling study. *Limnology and Oceanography*, 62(6), 2629–2649. <https://doi.org/10.1002/lno.10595>
- Rowe, M. D., Anderson, E. J., Wang, J., & Vanderploeg, H. A. (2015). Modeling the effect of invasive quagga mussels on the spring phytoplankton bloom in Lake Michigan. *Journal of Great Lakes Research*, 41, 49–65. <https://doi.org/10.1016/j.jglr.2014.12.018>
- Saha, S., Moorthi, S., Wu, X., Wang, J., Nadiga, S., Tripp, P., et al. (2014). The NCEP climate forecast system version 2. *Journal of Climate*, 27(6), 2185–2208. <https://doi.org/10.1175/JCLI-D-12-00823.1>
- Salmon, J. E., Holthuijsen, L. H., Zijlema, M., van Vledder, G. P., & Pietrzak, J. D. (2015). Scaling depth-induced wave-breaking in two-dimensional spectral wave models. *Ocean Modelling*, 87, 30–47. <https://doi.org/10.1016/j.ocemod.2014.12.011>
- Schoen, J. H., Stretch, D. D., & Tirok, K. (2014). Wind-driven circulation patterns in a shallow estuarine lake: St Lucia, South Africa. *Estuarine, Coastal and Shelf Science*, 146, 49–59. <https://doi.org/10.1016/j.ecss.2014.05.007>
- Schwab, D. J. (1983). Numerical simulation of low-frequency current fluctuations in Lake Michigan. *Journal of Physical Oceanography*, 13(12), 2213–2224. [https://doi.org/10.1175/1520-0485\(1983\)013%3C;2213:NSOLFC%3E;2.0.CO;2](https://doi.org/10.1175/1520-0485(1983)013%3C;2213:NSOLFC%3E;2.0.CO;2)
- Schwab, D. J., & Beletsky, D. (2003). Relative effects of wind stress curl, topography, and stratification on large-scale circulation in Lake Michigan. *Journal of Geophysical Research*, 108(C2), 3044. <https://doi.org/10.1029/2001JC001066>
- Schwab, D. J., & Morton, J. A. (1984). Estimation of overlake wind speed from overland wind speed: A comparison of three methods. *Journal of Great Lakes Research*, 10(1), 68–72. [https://doi.org/10.1016/S0380-1330\(84\)71808-9](https://doi.org/10.1016/S0380-1330(84)71808-9)
- Smagorinsky, J. (1963). General circulation experiments with the primitive equations: I. The basic experiment. *Monthly Weather Review*, 91(3), 99–164. [https://doi.org/10.1175/1520-0493\(1963\)091%3C;0099:GCEWTP%3E;2.3.CO;2](https://doi.org/10.1175/1520-0493(1963)091%3C;0099:GCEWTP%3E;2.3.CO;2)
- Soulsby, R. (1997). Combined waves and currents. *Dynamics of marine sands. A manual for practical applications*, (pp. 87–95). London, UK.: Thomas Telford Publishing.



- Strub, P. T., & Powell, T. P. (1986). Wind-driven surface transport in stratified closed basin: Direct versus residual circulations. *Journal of Geophysical Research*, 91(C7), 8497–8508. <https://doi.org/10.1029/JC091iC07p08497>
- Svendsen, I. A., Haas, K., & Zhao, Q. (2002). Theoretical background. *Quasi-3D nearshore circulation model SHORECIRC, user's manual*, Version 2.0 (5–21). Newark: Center for Applied Coastal Research, Department of Civil Engineering, University of Delaware.
- Thornton, E. B., & Guza, R. T. (1983). Transformation of wave height distribution. *Journal of Geophysical Research*, 88(C10), 7183–7192.
- Troitskaya, E., Blinov, V., Ivanov, V., Zhdanov, A., Gnatovsky, R., Sutyryna, E., & Shimaraev, M. (2015). Cyclonic circulation and upwelling in Lake Baikal. *Aquatic Sciences*, 77(2), 171–182. <https://doi.org/10.1007/s00027-014-0361-8>
- van der Westhuysen, A. J. (2010). Modeling of depth-induced wave breaking under finite depth wave growth conditions. *Journal of Geophysical Research*, 115, C01008. <https://doi.org/10.1029/2009JC005433>
- Wu, T., Qin, B., Ding, W., Zhu, G., Zhang, Y., Gao, G., et al. (2018). Field observation of different wind-induced basin-scale current field dynamics in a large, polymictic, eutrophic lake. *Journal of Geophysical Research: Oceans*, 123, 6945–6961. <https://doi.org/10.1029/2018JC014040>
- Xue, P., Pal, J. S., Ye, X., Lenters, J. D., Huang, C., & Chu, P. Y. (2017). Improving the simulation of large lakes in regional climate modeling: Two-way lake–atmosphere coupling with a 3D hydrodynamic model of the Great Lakes. *Journal of Climate*, 30(5), 1605–1627. <https://doi.org/10.1175/JCLI-D-16-0225.1>
- Zijlema, M. (2010). Computation of wind-wave spectra in coastal waters with SWAN on unstructured grids. *Coastal Engineering*, 57(3), 267–277. <https://doi.org/10.1016/j.coastaleng.2009.10.011>